Optimal Design of a Hydro-Mechanical Transmission Power Split Hybrid Hydraulic Bus

A dissertation

SUBMITTED TO THE DEPARTMENT OF MECHANICAL ENGINEERING,

UNIVERSITY OF MINNESOTA

BY

Muhammad Iftishah Ramdan

IN PARTIAL FULFILLMENT OF THE REQUIREMENTS FOR THE DEGREE OF DOCTOR OF PHILOSOPHY

Adviser: Professor Kim A. Stelson

December 2013

Copyright

Acknowledgements

First and foremost, I would like to express my deepest gratitude to Professor Kim A. Stelson for his guidance and patience during his years as my adviser.

I would like to express my sincere appreciation to my entire family - my wife, my mother, and siblings, for their endless moral support and for always believing in me.

Dedication

This thesis is dedicated to my father who succumbed to COPD, caused in part by the air

pollution in Malaysia. I hope my work could be one of the steps towards improving the

environment and the public health situation both in my native country and abroad.

Abstract

This research finds the optimal power-split drive train for hybrid hydraulic city bus. The research approaches the optimization problem by studying the characteristics of possible configurations offered by the power-split architecture. The critical speed ratio (S_{crit}) is introduced in this research to represent power-split configurations and consequently simplifies the optimal configuration search process. This methodology allows the research to find the optimal configurations among the more complicated dual-staged power-split architecture. The search for optimal single-staged and dual-staged power-split configurations is done by tuning the S_{crit} values until the optimal configuration is reached. The configuration candidates are simulated over three city bus drive cycles and to ensure they operate at optimal condition at each drive cycle, a dynamic programming is used. This study also establishes that there are two kinds of power re-circulation modes and one of them has a usable range with better efficiency than the series hybrid hydraulic architecture. A configuration candidate from single-staged power-split architecture is chosen to be the optimal drive train. The S_{crit} value of the optimal configuration is used to determine how all the gears in the optimal power-split HHB drive train are connected and the planetary gear ratio so that the physical drive train can be built.

Table of Contents

List of tables

List of figures

Nomenclatures

CNG   compressed natural gas

CBD   central Business District

CVT   continuously variable transmission

HHB/HHV   hybrid hydraulic bus/ hybrid hydraulic vehicle

HEB/HEV   hybrid electric bus/ hybrid electric vehicle

HMT   Hydro-mechanical transmission

HPR   hydraulic power re-circulation

HPA   high pressure accumulator

h   planetary gear ratio $\left(h = \frac{R}{S} \right)$

LPA   low pressure accumulator

ω_{input} input shaft angular/rotary speed

τ_{inout} input shaft torque

ω_x x = [sun, ring, carrier] gear angular speed

τ_x x = [sun, ring, carrier] gear torque

ω_{PM2} pump/motor 2 angular speed

ω_{PM1} pump/motor 1 angular speed

ω_{FD} final drive shaft angular speed

ω_{rat} vehicle speed ratio $\left(\omega_{rat} = \frac{\omega_{FD}}{\omega_{input}} \right)$

T_{PM2} hydraulic pump/motor 2 torque

T_{PM1} hydraulic pump/motor 1 torque

R	ring gear teeth count
S	sun gear teeth count
MPR	mechanical power re-circulation
P_h	hydraulic power ratio
PM	hydraulic pump/ motor
P_{mech}	mechanical power ratio
Q_x	flow of x, x = [HPA, system, PM1 or PM2]
SOC	state of charge
S_{crit}	critical speed ratio
ω_{rat}	speed ratio
γ	gear ratio
$\eta_{mech.}$	mechanical efficiency
$\eta_{hyd.}$	volumetric efficiency
η_x	efficiency of x, x = [engine, transmission, overall]
ω_{in} or ω_{out}	input or output shaft angular speed
t_x	simulation time x = [initial, final]

Chapter 1

Motivation and objective

Public transportations move large numbers of people with minimal space that helps to reduce traffic congestions and consequently reduce nation's energy consumption. In 2010, in the United States, the public transit saved drivers $16.8 billion in gasoline consumption and traffic congestion time [9]. Their effectiveness is shown by the increase in demands that between 2004 and 2011, the use of public transportations increased by 12% (while population rate grew 6%). More than half of these users chose city buses as their transportation mode [9].

Figure 1.1. Example of how much space saved by using bus (httpwww.outsidethebeltway.com)

The city bus discussed is a 12.2 meter (40 feet) long, capable of carrying 38 seated and 33 standing passengers. The bus is categorized as a heavy-duty vehicle, usually powered by a diesel engine that operates on fixed routes, often subjected to low-speed with national average speed of 5.8 m/s (12.9 mph) [8], and high-frequency stop-and-go driving conditions. These driving conditions result in high fuel consumption and emissions.

Figure 1.2. Example of 40 ft city bus (httpwww.metrotransit.org)

The increasing demand for city buses and their operation in densely populated areas poses a public health hazard. In 2006, buses and heavy trucks accounted for a third of NOx emissions and a quarter of PM emissions [40]. Starting in 2007, the United States Environmental Protection Agency (USEPA) has issued more stringent regulations on heavy-duty vehicle emissions by requiring all diesel engines to emit no more than 0.01 grams particulate matter (PM) per brake horsepower-hour (g/bhp-hr) [40]. These strict EPA regulations, along with increased crude oil prices, have been the key driving force behind the emergence of new city bus technologies, namely, compressed natural gas (CNG) and hybrid electric buses (HEB).

Current conventional diesel buses are equipped with highly efficient diesel engines, running on ultra low sulfur diesel (ULSD) fuel, and equipped with particulate matter filters systems ($4000~$8000 each) to meet the EPA emission regulations [8]. Although particulate matter filters need frequent replacement, conventional diesel buses are still the cheapest among the three. The CNG bus offers similar fuel economy to that of the conventional diesel bus, but the fuel is cleaner than the diesel, thus eliminating the need for a PM filter. The natural gas has to be compressed prior to use, which requires additional costs in energy for gas compression and special infrastructure for fueling station and depot modification. The median cost for fueling station and depot modification are $2 million and $875,000 respectively [8].

The HEB offers the best fuel economy among the three because of its ability to recuperate braking energy, use of optimized control strategy and downsized engine. However, the use of the electric systems in heavy-duty vehicles is not desirable due to high procurement and maintenance costs, low power density and reliability issues. The HEB procurement cost is $531,605, while the conventional diesel and the CNG buses costs are $319,709 and $ 342,366, respectively. The HEB maintenance cost is heavily influenced by its battery short lifecycle. The HEB has the choice to be equipped with either acid battery that costs $25,000 and needs to be changed every three years, or NiMH battery that costs $35,000 to $45,000 that would last for 5 to 7 years [8]. The battery also needs to be conditioned every six months by the battery conditioner that costs $70,000.

Table 1.1 Fuel economy improvements offered by the HEB [46]

	Manhattan (mpg)	NYC (mpg)	CBD (mpg)
Conventional	1.46	1.4	2.19
HEB	2.56	2.3	3.25
Fuel economy improvements	75.3 %	64.3%	48.4%

In vehicle designs, the drive train components are sized depending on the vehicle power demand. A heavy duty vehicle like a city bus needs high power to accelerate to overcome its large inertia. Since the battery has low power density, the battery needed to be installed in the city bus is unreasonably big and heavy. Thus, HEB is equipped with battery that is rated less than the vehicle power demand. To ensure the longevity of the battery life, the amount of power allowed to be absorbed by the battery is limited and the battery SOC has to be maintained around 70% to 75% [1].

A city bus needs a durable, efficient and cost-effective hybrid drive train and a hydraulic hybrid could be an appropriate alternative. The hybrid hydraulic bus (HHB) stores energy in a high power density high pressure hydraulic accumulator eliminating any of the mentioned battery issues. While the HEB power flow are limited to ensure the longevity of the battery life, the hydraulic accumulator allows most of the braking power to be absorbed and released without damaging its reliability. Like the HEB, the HHB also has some drawbacks. Its energy storage (hydraulic accumulator) is less energy dense than an electric battery and its motor has a lower speed limit (but has much higher low end torque) than its electric counterpart. However, for a heavy-duty city bus with low-speed, high-frequency stop-and-go duty cycles, having a high-power density system with a high low-end torque is more important than having a high-energy density with a high-speed drive train. These differences in physical properties between the electric and hydraulic hybrid components show the HHB design needs to be optimized differently than the HEB.

There are three hydraulic hybrid drive train architectures, namely: parallel, series and power-split. The parallel is the simplest architecture as it assists the conventional drive train by storing and releasing excessive kinetic energy as needed. It does not allow for the full control of

the engine, but it uses a high-efficiency mechanical transmission. The series architecture is a hydrostatic transmission with high- and low-pressure hydraulic accumulators placed between two pump/motors (PM) as a means to store energy. There is no mechanical connection between the engine and the output shaft, thus allowing full engine control, but resulting in double power conversion that lowers the transmission efficiency. The power-split architecture splits the input power into two power paths, allowing for both full engine control and efficient power transfer. The power-split architecture is also known as the Hydro-mechanical Transmission (HMT) when hydraulic components are used. Adding hydraulic accumulators into the HMT creates a hydraulic hybrid drive train that allows energy storage capacity. This architecture is very sensitive to the design and the control strategy since it is more complex compared to the other two. This research focuses on the optimized design and control strategy of the power-split hybrid architecture for a city bus.

HMTs are widely used in off-road and agricultural vehicles due to their reliability, smoothness, and high-efficiency power transfer [16] [29]. A conventional HMT uses at least one planetary gear set (PGS) that consists of sun, carrier and ring gears. Different ways of connecting these gears create different configurations. A dual staged (or compound) HMT uses two planetary gear sets, resulting in 1,152 possible configurations [24]. A single-stage HMT (or simple HMT) uses one planetary gear set, resulting in twelve possible configurations, which makes it much cheaper to make and simpler to control than a compound one. The drawback behind its simplicity is that a simple HMT can run in the inefficient power re-circulation mode while the dual-staged HMT could avoid that. A non-conventional HMT does not use any planetary gears. Instead, it uses special kind of hydraulic PM that allows its housing to slip. Thus, the power is split and combined using the difference in the PM input shaft and its housing speeds. Its compact design makes it popular among low-power applications such as in

Hondamatics transmission in Honda light-duty vehicles [16] and in Cessna landing gear transmission [50].

This research approached the HHB optimization problem from the angle of conventional HMT possible configurations and their kinematic characteristics. Thus, unlike most HMT optimization studies done to date, which use the Prius or reversed-Prius power-split configuration as the platform to simply optimize the components' sizes and control strategy, this research investigates the kinematic properties of different HMT configurations. This starting method is needed to be a general methodology for any HMT drive train design because the optimized HMT configuration is different depending on the vehicle applications. The expected result from this research would be an optimized HMT drive train that is designed exclusively for a heavy-duty city bus application that later can be used as an efficient and reliable mode of public transportation.

Chapter 2

Study background

A number of technical papers published dynamometer testing results, comparing the fuel economies of electric hybrid, conventional diesel, and CNG buses, and establishing the superior fuel economy (and reduced emissions) of the electric hybrid buses (HEB) [1][8]. The average HEB fuel economy is 3.14 MPG while conventional diesel and CNG buses' average fuel economy is 2 MPG on Manhattan drive cycle [1]. The fuel economy improvements might not look very impressive for a passenger car, but it is a big leap for a bus that can potentially carry 68 people. A hybrid drive train's ability to recuperate energy and improve the engine's operating efficiency has clearly proven to be effective in city bus applications. However, as stated before, the electric hybrid technology in a heavy-duty application is too expensive to implement.

The hydraulic hybrid system offers high power density, performance consistency, and better cost effectiveness than the electric counterpart [32]. While the charging/discharging rate is limited in HEB, the high power density in hydraulic accumulator allows both high frequency and high rates of charging/discharging while keeping HHB weight reasonable [14]. As a result, the hydraulic hybrid drive train is capable of regenerating more than seventy percent of the braking power as opposed to less than twenty-five percent for the same size electric hybrids [19]. Moreover, the fact that a hydraulic motor can be stalled without being damaged [32] makes hydraulic hybrid system a reliable option to work at high torque and low speed conditions like those usually experienced by heavy-duty city bus. Unlike the electric battery, the

performance of the hydraulic energy storage (i.e. the accumulator) does not deteriorate due to braking frequency or age, which eliminates high maintenance costs. The HHB periodic maintenance cost should be comparably lower than the HEB because the hydraulic system is a type of a mechanical system that any mechanic should be able to do the maintenance work on it.

Heavy-duty city bus operation involves high power transfer meaning high amount of heat is generated, which needs to be dissipated. HEB hybrid system is equipped with cooling system to control the traction batteries' temperature. In summer weather, however, HEB are reported to experience 'thermal foldback', when the traction batteries become too hot and the hybrid control system reduces power to help the hybrid system to cool the battery. During the thermal foldback, the hybrid system is not able to regenerate the braking power and the fuel economy is greatly affected because technically, the HEB becomes an overweight conventional diesel bus [45]. Since the hydraulic system is interconnected by fluid, heat from every component is effectively transferred by the hydraulic fluid and can be dissipated at a heat exchanger [32]. Furthermore, the hydraulic fluid viscosity can be changed, depending on the season, to ensure the hydraulic system works at optimal condition.

The hydraulic system, however, has some disadvantages, compared to the electric counterparts. Its accumulator is referred to as a short-term storage system [14] because it has low energy density such that it can never be the sole energy source for the drive train. The hydraulic pump/motor has a much lower speed limit compared to electric generator/motors. These two shortcomings should not affect the fuel economy of HHB since the city bus often operates at low speed and high-frequency stop-and-go conditions. Other than that, the hydraulic system is infamous of being noisy and the nitrogen gas in accumulator would permeate the hydraulic fluid and needs periodic recharge. The noise problem can be handled by

proper insulations or cabin noise cancelling. The accumulator needs of periodic nitrogen re-charging and should be still cheaper than the battery conditioning and replacement.

The hydraulic hybrid exists in the forms of parallel, series, and power-split architectures. The parallel hydraulic hybrid is the easiest to adapt from an existing conventional drive train, as has been demonstrated by full-production hydraulic hybrid refuse trucks, joint-ventured by Peterbilt and Eaton [19]. Bosch Rexroth's manufactures the parallel architecture Hydrostatic Regenerative Brake (HRB) system as an add-on braking system [19]. These have demonstrated a fifteen- to thirty-percent improvement in fuel economy, primarily by means of regenerated braking energy and a highly efficient power transfer.

The series architecture is also used in heavy-duty hybrid hydraulic vehicles (HHV) and offers superior fuel economy to that of the parallel architecture in city drive cycles. The EPA published the results of lab tests run on EPA series HHV, with fuel economy improvement of up to 119% on the Manhattan city bus drive cycle [19]. This is due to the fact that, in addition to regenerative braking, the series architecture is able to work as a continuously variable transmission (CVT), allowing the engine to operate at high-efficiency conditions. It achieves the CVT functionality by decoupling the mechanical connection between the engine and the final drive. The mechanical decoupling also results in a low transmission efficiency, which is reflected in bad fuel economy when regenerative braking cannot be utilized. At a constant speed, the low transmission efficiency can be evident as the fuel economy decreases by fourteen percent when the series architecture operates using the highway drive cycle [8].

Parker Hannifin developed a series hydraulic hybrid called *RunWise* that allows mechanical direct drive at highway speed to avoid the mentioned low efficiency problem. This drive train is used in lightweight Altair BUSolution LTO 140 city bus and claimed to achieve fuel economy of 6.9 MPG on ABD drive cycle (combination of CBD, arterial and commuter drive

cycles) [17]. By comparison, Altoona bus research and test center published fuel economy of buses going through ABD drive cycle; a conventional diesel bus averages about 3.3 MPG, Gilig GM/Allison HEB and New Flyer HEB XDE40 achieve 4.74 MPG and 5.34 MPG, respectively [17]. The Altair series HHB was designed from scratch and significantly reduces its weight by optimized monocoque structure, resulting in weight of only 11702 kg (Orion VII HEB weighs 13732 kg). The fuel economy achieved by the Altair HHB is impressive and proves that a carefully designed HHB is able to achieve better fuel economy than the HEB.

The power-split hybrid architecture's fuel economy should, in theory, be superior to the other two architectures' because it combines the advantages of high efficiency power transfer and CVT control freedom at any speed. The engine power is split at the input shaft into the hydraulic and the mechanical power paths and recombined at the power output shaft. Unlike *RunWise* series hybrid drive train that uses high efficiency mechanical drive only at highway speed, the HMT drive train can be designed such that it would utilize high transmission efficiency from the mechanical power path at low speed city driving condition.

The splitting and the combining process in HMT conventionally require at least one PGS. A dual-staged HMT requires two PGS, while the single-staged needs only one. There are a total of twelve possible single-stage HMT configurations [37] and 1152 for dual-staged/compound-coupled HMT [24]. The single-staged HMT is simpler, but susceptible to low-efficiency power re-circulation. The dual-staged HMT is able to avoid the power re-circulation modes but is more complex to control and optimize. An attempt to optimize the dual-stage HMT has been made [24], but that proved to be markedly time-consuming.

Power re-circulation mode has always been viewed as inefficient, and to be avoided at all costs [28]. This study shows that there are actually two types of power re-circulation: hydraulic power re-circulation (HPR) and mechanical power re-circulation (MPR). The HPR

happens when the power at the hydraulic power path is reversed to feed power into the mechanical power path. Thus, the mechanical power path carries a larger amount of power than is input by the engine. This type of power re-circulation is usable to some extent because, as the later chapters reveal, its efficiency could actually be higher than the series architecture efficiency. The MPR, on the other hand, happens when the power at the mechanical power path is reversed, thus adding extra power into the inefficient hydraulic power path. This mode is very inefficient and can be avoided by drive train design.

Many studies done on power-split drive trains involve the size optimization and the control strategy of the Prius or the reversed Prius configurations [25, 33, 42]. While these configurations might work well in light-duty vehicles, they might not necessary be optimal in heavy-duty applications, such as a city bus. This research intends to design the optimal drive train of a Hybrid Hydraulic Bus (HHB) by investigating all twelve basic configurations of single-staged HMT and also ventures a look into the dual-staged HMT configurations.

A configuration classification system was developed for the twelve different single-staged HMT configurations, based on how the planetary gear set members are connected to the PM units and to the input or the output shafts [37]. There are two types of single-staged HMT, the input-coupled and the output-coupled. The input-coupled type places the fixed gear coupling at the input side and the planetary gear set at the output side of the HMT. The output-coupled type places the fixed gear coupling at the output side and the planetary gear set at the input side of the HMT. Each of these twelve HMT configurations has its own power management characteristics in response to speed ratios. The HMT physical configurations are later proven to be not unique [6] and the non-uniqueness property is further applied to create two generalized HMT equations. The general equations are used to find the critical speed ratios in this research that further simplify the HMT configurations' choosing process.

Chapter 3

Energy analysis in drive cycle

3.1. City bus drive cycles

A drive cycle is a set of speed (and gradient) arrays with respect to time, derived from recorded data of a specific vehicle driven on a specific route. It usually used in dynamometers and simulations to test a vehicle's emissions and fuel economy. It also provides valuable information about the vehicle's typical speed and acceleration. Three heavy-duty city vehicle drive cycles, Central Business District (CBD), New York City (NYC), and Manhattan (fig. 3.1), are used to represent city bus driving conditions. The acceleration and the speed throughout the drive cycles are used to determine the effectiveness of the hydraulic hybrid energy recuperation feature in a vehicle.
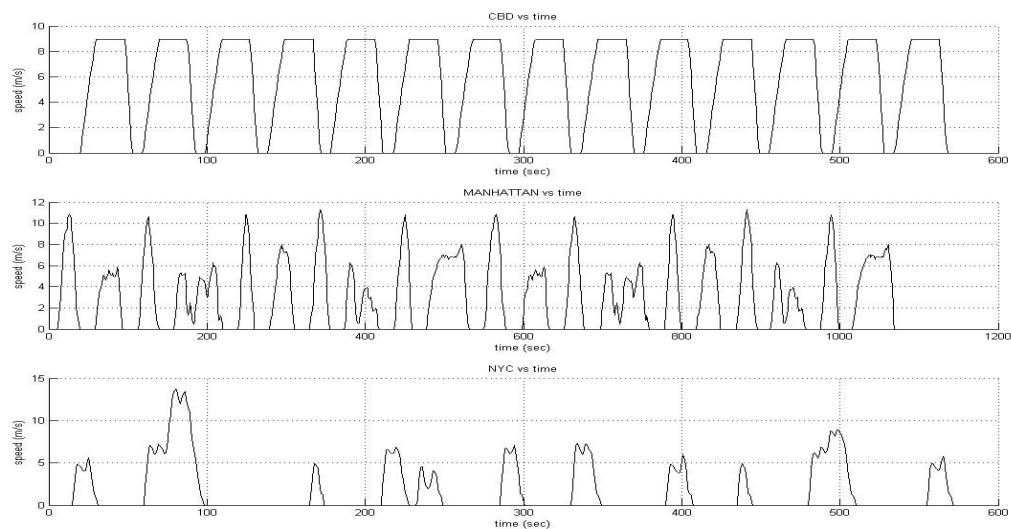
Figure 3.1. Three city bus drive cycles used in the research

The Central Business District (CBD) drive cycle was created by the US Department of Transportation (USDOT) and the Urban Mass Transit Association (UMTA) and is widely used in chassis dynamometer bus performance testing procedures. It has a saw-tooth profile consisting of fourteen cycles of idle, acceleration, cruise and deceleration. The Manhattan drive cycle is synthetic, compiled using data collected from the Orion-LMCS Hybrid Electric Bus (HEB) and conventional diesel buses travelling on several different New York Metropolitan Transit Authority (NY MTA) bus routes. The data consist of 112 HEB micro-trips and 287 conventional diesel bus micro-trips. The micro-trips are then randomly combined until their mean and standard deviation values become similar to the original ones (before the combination took place). The New York City drive cycle data were collected from city buses and heavy-duty trucks driven in mid-town Manhattan. The data consist of rapid stop-and-go traffic with long passenger transfer times.

Table 3.1. Three city bus drive cycles summary

City bus drive cycles	Ave. speed (m/s)	Max. speed (m/s)	Max. acceleration (m/s^2)
CDB	3.14 (7.03 mph)	8.94 (20 mph)	1.03
Manhattan	2.14 (4.78 mph)	11.31 (25.3 mph)	2.06
NYC	2.25 (5.02 mph)	13.77 (30.8 mph)	2.77

The three drive cycles show city bus often operates at speed below the city 30 mph limit. Despite the low speed, they show high rate and high frequency stop-and-go driving pattern with maximum acceleration of 2.77 m/s^2. This translates to high power demand during the acceleration and high power loss in deceleration events with subsequent high fuel consumption (refer appendix b.). The hybrid system is designed to absorb the otherwise wasted

kinetic energy while braking and use it during the acceleration to reduce the internal combustion engine energy usage.

3.2 Energy analysis

The hybrid system in HEB and HHB adds extra weight to the vehicle, which requires high energy to operate. However, both hybrid electric and hydraulic buses have energy recuperation capability that compensates for the energy requirement due to the added weight. The energy analysis is meant to estimate how effective the energy that can potentially be saved by both hybrid buses is.

3.2.1 Hybrid buses mass

Since there is no HMT hybrid bus in production, the HMT bus mass is based on the Orion VII HEB with the mass of its hybrid electric components taken out and replaced by the hydraulic components (table 3.2). Altair produced a lightweight series HHB that only weighs 11,702.7 kg, just slightly heavier than the Orion VII conventional diesel bus. The mass of the HMT bus is not based on the Altair HHB because it was specially designed for the simpler series architecture and might not be able to fit the more complex HMT drive train.

Table 3.2: Four buses mass comparisons

Bus types	Mass with 27 passengers (kg)	% addition mass from Orion VII diesel
Orion VII Conventional diesel	13,370	--
Orion VII Hybrid Electric bus	15,570	16.5
HMT Hybrid Hydraulic bus	14,783	3.4
Altair BUSolution LCO 140	13,538	1.26

3.2.2 Mean tractive force

Energy analysis starts with the mean tractive force. Any object with wheels has to overcome four forces to accelerate. They are: aerodynamic drag (F_{aero}), inertial mass ($F_{inertia}$), gradient force (F_g) and rolling resistance (F_{rr}). Newton's second law represents longitudinal vehicle dynamics (eq. 3.1).

$$m_v \frac{d}{dt} v(t) = F_{traction} - (F_{aero}(t) + F_{rr}(t) + F_g(t)) \tag{3.1}$$

Re-writing Newton's second law yields the tractive force needed to propel (eq. 3.2).

$$F_{traction} = m_v \frac{d}{dt} v(t) + F_{aero}(t) + F_{rr}(t) + F_g(t) \tag{3.2},$$

Which
$$F_{aero} = \frac{1}{2} \rho_{air} A_{frontal} C_d v^2$$

$$F_{rr} = C_{rr} m_v g \cos(\alpha)$$

$$F_g = m_v g \sin(\alpha) \approx m_v g \, \alpha$$

$$F_{inertia} = m_v \frac{d}{dt} v(t) = m \, a$$

The mean tractive force is the mean effort needed to follow the drive cycle, also equal to the average energy consumed per distance travelled. It is a good measurement to estimate how much energy could be potentially saved on average if the hybrid system is used. The calculation of the mean tractive force is different for the three vehicles due to different weights and energy recuperation abilities. Since the gradient angles (α) for all three drive cycles are zero, the gradient gravitational force (F_g) can be ignored.

A. <u>Mean tractive force of conventional bus</u>

For a conventional diesel city bus, energy is spent mainly during acceleration and cruising at constant speed. Thus, the mean traction force is only calculated when the bus is accelerating and cruising (eq. 3.3).

$$\bar{F}_{traction} = \frac{1}{(total\ distance)} \int_{t=t_{accel.+cruise.}}^{t_0} F(t)\ v(t)dt \qquad (3.3)$$

Or, in discretized form:

$$\bar{F}_{traction} = \frac{1}{(total\ distance)} \Sigma_{i\in accel.+cruise.} F_{traction(C)i},\ \bar{v}_i\ \Delta t \qquad (3.4)$$

Where Δt is the time step. The mean speed and acceleration at every time interval is as follows:

$$\bar{v}_i = \frac{v_i+v_{i-1}}{2} \qquad\qquad \bar{a}_i = \frac{v_i-v_{i-1}}{\Delta t}$$

The mean traction force for the conventional diesel city bus is the sum of aerodynamic drag, rolling resistance and inertial forces (eqs. 3.5 – 3.8).

$$\bar{F}_{aero} = \frac{1}{distance} \left(\frac{1}{2} \rho_{air} A_{frontal} C_d\right) \Sigma_{i\in accel.+cruise.} \bar{v}_i^{\ 3} \Delta t \qquad (3.5)$$

$$\bar{F}_{rr} = \frac{1}{distance} (C_{rr}\ m_v g \cos(\alpha)) \Sigma_{i\in accel.+cruise.} \bar{v}_i \Delta t \qquad (3.6)$$

$$\bar{F}_{inertia} = \frac{1}{distance}\ m_v \Sigma_{i\in accel.+cruise.} \bar{a}_i\ \bar{v}_i \Delta t \qquad (3.7)$$

$$\bar{F}_{traction(C)} = \bar{F}_{aero} + \bar{F}_{rr} + \bar{F}_{inertia} \qquad (3.8)$$

B. Mean tractive force of Hybrid buses

Hybrid buses have the ability to recuperate energy, but are heavier than their conventional counterparts. Since energy is absorbed during deceleration, the mean tractive force calculation covers the entire time range and not just when accelerating and cruising (eq. 3.9 - 3.12). The mean tractive force during deceleration event should ideally cancel out the mean tractive force during acceleration event. In the mean tractive force equation, the decelerating mean force term is multiplied by the recuperation efficiency ($\eta_{recup.}$) to show that in real life, not all of the deceleration energy is absorbed and reused (eq. 3.12). Due to the high power density, the hydraulic system allows a high rate of energy to go through it while the electric hybrid system does not. EPA reports the hydraulic hybrid system is capable of producing 70%$\eta_{recup.}$, while for the electric hybrid only achieve 25% $\eta_{recup.}$ [19].

$$\bar{F}_{aero} = \frac{1}{distance} \left(\frac{1}{2} \rho_{air} A_{frontal} C_d \right) \sum_{i=1}^{n} \bar{v}_i^3 \Delta t \qquad (3.9)$$

$$\bar{F}_{rr} = \frac{1}{distance} \left(C_{rr} \left(m_{v(HHB \, or \, HEB)} \right) g \cos{(\alpha)} \right) \sum_{i=1}^{n} \bar{v}_i \Delta t \qquad (3.10)$$

$$\bar{F}_{inertia(accel.+cruise.)} = m_v \frac{d}{dt} v(t) = \frac{1}{distance} \left(m_{v(HHB \, or \, HEB)} \right) \sum_{i \in accel.+cruise.} \bar{v}_i \, |\bar{a}_i| \, \Delta t$$

$$(3.11)$$

$$\bar{F}_{inertia(decel)} = m_v \frac{d}{dt} v(t) = \frac{1}{distance} \left(m_{v(HHB \, or \, HEB)} \right) \sum_{i \in decel} \bar{v}_i \, \Delta t \, |\bar{a}_i| \, \eta_{recup}. \qquad (3.12)$$

$$\bar{F}_{traction(H)} = \bar{F}_{aero} + \bar{F}_{rr} + \bar{F}_{inertia(accel.+cruise..)} - \bar{F}_{inertia(decel.)} \qquad (3.13)$$

3.3 Average energy analysis results

Comparison between the three types of city buses is done by calculating the mean tractive forces the buses need in the three drive cycles. The mean tractive forces are calculated with the HHB and HEB equipped with 70% and 25% energy recuperation efficiency, respectively. The masses of buses are different in the calculation, as shown in table 3.2. The mean tractive force for HHB are calculated in two cases, one is the case if the HHB mass is based on the Orion VII HEB and the other one is the case if the mass of the HHB is as lightweight as the Altair bus.

Table 3.3: Mean tractive force for four buses on three drive cycles

Drive cycle	Bus	Mean traction force (N)	% energy per distance saved
Manhattan	Conventional	4,225	--
Manhattan	HEB	4,187	0.9
Manhattan	Orion VII HMT	2,109	50.1
Manhattan	Altair HHB	1,946	53.9
CBD	Conventional	3,099	--
CBD	HEB	2,985	3.7
CBD	Orion VII HMT	1,692	45.4

17

CBD	Altair HHB	1,570	49.3
NYC	Conventional	5,424	--
NYC	HEB	5,362	1.1
NYC	Orion VII HMT	2,567	52.7
NYC	Altair HHB	2,367	56.4

% Energy per distance saved $= \frac{(\bar{F}_{traction(C)} - \bar{F}_{traction(H)})}{\bar{F}_{traction(C)}} 100\%$ (3.14)

Table 3.3 shows the mean tractive force and percentage of average energy saved by all the buses mentioned (eq. 3.14). According to the table, both HHBs benefit the most from the NYC drive cycle and the least from the CBD drive cycle. This is due to its high recuperation efficiency that allows it to obtain high energy from the drive cycle with the highest acceleration and deceleration (NYC). The HEB, on the other hand, could not benefit as much due to its low recuperation efficiency and heavier weight. The lightweight Altair HHB achieves slightly better performance over the standard weight HHB.

This chapter answers the question about the effectiveness of the two hybrid buses. The hybrid system uses the inertial force to its advantage, absorbing the inertial energy and releasing it as needed. The HHB is heavier than the conventional bus due to the addition of high- and low-pressure accumulators and two units of PMs. In the case of a city bus that is heavy to begin with, the hybrid components only adds 3.4% to the original mass. On the other hand, the HEB is 16.5% heavier than the conventional bus due to the heavier high-power battery and motors/generators. The HEB higher weight and low recuperation efficiency shows it saves a good amount of energy at the drive cycle with mild acceleration (CBD), but saves very little energy for more aggressive drive cycles (Manhattan and NYC). This chapter also estimates the Orion VII based HHB should achieve similar fuel economy from the lightweight Altair HHB.

Chapter 4

Parameter study and drive train sizing

A drive train consists of an engine, a transmission, and speed reducers (fig. 4.1). Speed reducers are fixed-ratio gears, placed between the engine and the transmission (GR1), and between the final drive shaft and the wheel shaft (GR2). This chapter shows the first iteration of the drive train design, treating the HMT as a transmission (without considering the hybrid power recuperating system), to determine the gear ratios of speed reducers GR1 and GR2.
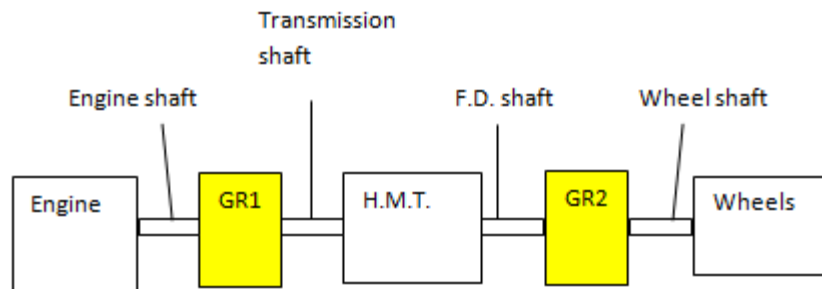
Figure 4.1. General HMT drive train structure

A gear ratio, by definition, is the ratio between the input speed and the output speed of a drive train system. By the conservation of power, the torque ratio is the reciprocal of the gear ratio (eq. 4.1)

$$\gamma = gear\ ratio = \frac{\omega_{input}}{\omega_{output}} = \frac{T_{output}}{T_{input}} \qquad (4.1)$$

The GR1 and GR2 gear ratios are meant to allow the vehicle to accelerate and to reach the maximum speed without making the engine or the transmission components operate at their torque and speed limitations (table 4.1).

Table 4.1. Physical limitations of engine and hydraulic pump/motor

Components	model	Speed limit (rad/s)	Torque limit (Nm)
Diesel engine	Caterpillar C-10 250 kW	219	1695
Hydraulic PM	A4VG250 250 cc/rev	282.7	1590

4.1 Vehicle top speed

The maximum speed of the bus is determined by the conservation of engine power. Assuming the bus is travelling at a constant speed (with empty charge in accumulator) on a flat road, neglecting the inertia and the gradient forces at maximum engine power (eq.4.2).

$$P_{\max\,(engine)} = F_{tract.} v_{max} = 250\ kW$$

(4.2)

$$P_{\max\,(engine)} = \left(\frac{1}{2}\ \rho_{air}\ A_{frontal}\ C_d\ v_{max}^2 + C_{rr}\ m_v\ g \right) v_{max}$$

(4.3)

For the city bus, the predefined constants are:

$C_d = 0.79$

$\rho_{air} = 1.202\ \dfrac{kg}{m^3}$

$C_{rr} = 0.00475$

$A_{frontal} = 7.2413\ m^2$

$m_v = 14{,}783\ kg$

$R_{tire} = 0.5715\ m$ (Tire radius for 305/70 R 22.5)

With all the constants defined, eq. 4.3 is solved and the bus top speed is determined. The city bus is theoretically capable of reaching the maximum speed of 37.22 m/s (83.27mph) on a flat

20

surface. Since this calculation ignores any disturbance or inefficiency of the drive train, a coefficient of 0.7 is used to get a more realistic maximum speed achievable by the city bus. The maximum speed used in this study is $\left(37.22\ \frac{m}{s} \times 0.7 = 26.06\frac{m}{s}\right)$. Thus, without the help from a secondary power source, the 250kW diesel engine is expected to supply the power such that the bus would operate at speeds ranging from 0 m/s to 26.06 m/s (~60 mph), or at 45.59 rad/s wheel speed (Eq.4.4).

$$\omega_{wheel(max)} = \frac{v}{R_{tire}} = 45.59\frac{rad}{s} \qquad (4.4)$$

4.2 Equivalent gear ratio (GR_{eq})

The equivalent gear ratio is the overall drive train gear ratio that relates the angular speeds of the engine and the wheel drive shaft. It is also equals to the product of the gear ratios of all drive train components (eq. 4.5).

$$\gamma_{G_{eq}} = \frac{\omega_{engine}}{\omega_{wheel}} = \gamma_{GR1} \times \gamma_{HMT} \times \gamma_{GR2} \qquad (4.5)$$

There are two kinds of equivalent gear ratios, the high-speed and high-torque. These two equivalent gear ratios are used to determine both speed reducers' (GR1 and GR2) gear ratios that satisfy the drive train's physical limitation in two extreme cases, namely, high-speed and high-torque.

    a.   High-speed equivalent gear ratio $(\gamma_{eq(hi-spd.)})$

The high-speed equivalent gear ratio is the overall gear ratio when the last available gear is used for high-speed vehicle operations. This equivalent gear ratio is determined by taking the ratio of the engine's and the wheel shaft's maximum speed (eq. 4.6).

$$\gamma_{eq(hi-spd.)} = \frac{\omega_{e(max)}}{\omega_{wheel(max)}} = \frac{219.91}{45.59} = 4.823 \qquad (4.6)$$

    b.   High-torque equivalent gear ratio $(GR_{eq\ (hi-trq)})$

The high-torque equivalent gear ratio is the drive train overall gear ratio when the transmission is shifted to the first gear. The first gear in a transmission is designed to accommodate the high torque and low speed demand like when accelerating from zero speed. The high-torque equivalent gear ratio is defined by the ratio of maximum wheel torque to the maximum engine torque (eq. 4.7).
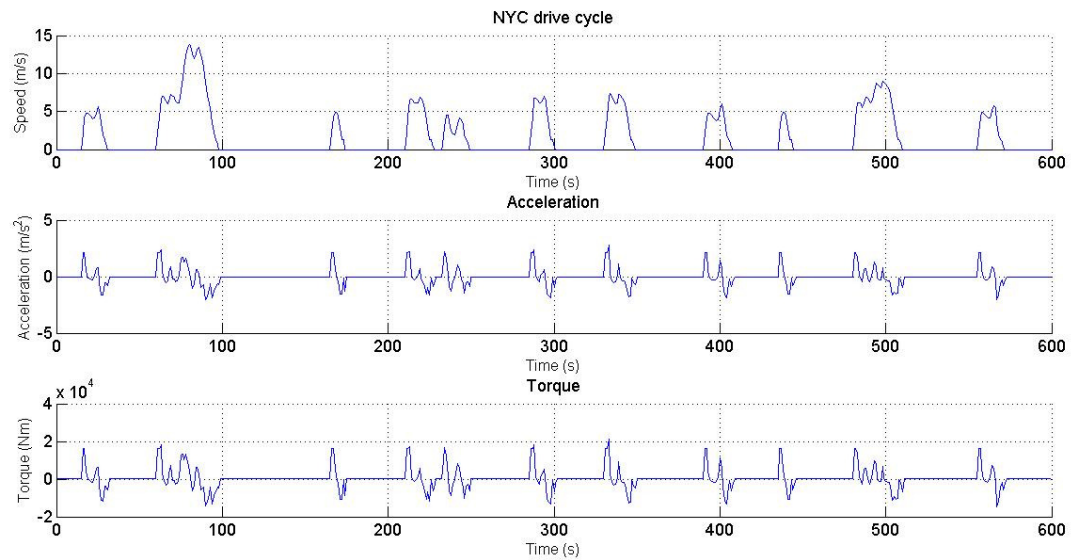
Figure 4.2. NYC city bus drive cycles speed, acceleration and torque

From chapter three, the maximum acceleration of 2.77 m/s/s was recorded from the NYC drive cycle at t = 333 s. The highest acceleration can be seen when the bus is starting to accelerate, or at a low speed of 7.063 m/s (15.8 mph) (fig. 4.2). The wheel torque needed at that point is 21,050 Nm, with the power demand of 239 kW while the maximum 250 kW engine torque is 1,695 Nm. Thus, the high torque equivalent gear ratio is determined (eq. 4.7).

$$\gamma_{eq(hi-trq.)} = \frac{T_{wheel(max)}}{T_{e(max)}} = \frac{21,050}{1,695} = 12.419 \hspace{2cm} (4.7)$$

It is worth mentioning that the maximum power demand happens at time t = 78, where the power demand is 303.4 kW. This clearly shows that the 250 kW engine cannot provide the power needed and a larger engine is usually used to accommodate the power demand. In the

22

HHB design, a slightly smaller engine, such as Caterpillar C-10 250 kW is intentionally used to reduce fuel consumption and extra power needed is supplied by the hybrid power source.

4.3 Gear ratios for HMT, GR1, and GR2.

A transmission is a variable gear ratio selector while a gear reduction is a fixed gear. In this sub-chapter (i. &ii.), the HMT gear ratio range and the speed reducers (GR1 and GR2) gear ratios are defined.

i.   <u>Hydro-mechanical transmission (HMT) gear ratio range</u>

The HMT is designed to have a speed ratio range similar to the commonly used conventional automatic city bus transmission, model ZF5HP590 (table 4.2). The speed ratio is the reciprocal of the gear ratio; $\text{speed ratio} = \frac{1}{\text{gear ratio}} = \frac{\omega_{output}}{\omega_{input}}$

Table 4.2.Gear ratios for a city bus automatic transmission ZF5HP590

Gears	1st	2nd	3rd	4th	5th
Gear ratio	3.43	2.01	1.42	1	0.83
Speed ratio	0.29	0.50	0.70	1	1.20

The hydrostatic transmission part of the HMT provides the CVT capability that allows seamless gear ratio shifting and drive train decoupling. Drive train decoupling allows the engine to idle while the vehicle is at zero speed, a task traditionally done by the clutch or the torque converter. By the definition of the speed ratio, $\left(\frac{\omega_{output}}{\omega_{input}}\right)$, the drive train decoupling means the speed ratio is zero. In the high-speed case, following the conventional transmission, the speed ratio is set to be 1.2. Thus, the HMT should allow the speed ratio to range from zero to 1.2.

$$0 < \frac{1}{\gamma_{hmt}} < 1.2 \qquad , \qquad 0 < \omega_{rat} < 1.2 \qquad\qquad (4.8)$$

      GR1 and GR2 speed reducers gear ratios

Previously, the high-torque and high-speed equivalent gear ratios, and the HMT gear ratio range, are determined. Thus, the gear ratios of both speed reducers can be calculated. The method of determining the gear ratios of the two speed reducers varies for different types of HMTs (input-and output-coupled).

a. Output-coupled HMT

The output-coupled HMT design mechanically couples the PM2 to the final drive shaft via the GR2 speed reducer. Thus, the GR2 gear ratio is designed such that the vehicle is allowed to travel at the maximum speed without PM 2 reaching its speed limit. The GR2 gear ratio is determined by dividing the maximum PM2 angular speed by the maximum wheel angular speed (eq. 4.9).

$$\gamma_{GR2-OC} = \frac{\omega_{PM2(max)}}{\omega_{wheel(max)}} = \frac{282.7}{45.59} = 6.202 \tag{4.9}$$

The GR1 gear ratio is determined by dividing the maximum engine speed by the maximum transmission input shaft speed (eq. 4.11). The GR1 gear ratio is obtained by using the definition of equivalent gear ratio (4.10). The high speed HMT gear ratio $(\gamma_{HMT(hi-spd)})$ from table 4.2 is used in this calculation.

$$\gamma_{eq(hi-spd.)} = \gamma_{GR2}\gamma_{GR1}\gamma_{HMT(hi-spd)} = 4.823 \tag{4.10}$$

$$\gamma_{GR1-OC} = \frac{\gamma_{eq(hi-spd.)}}{\gamma_{GR2}\gamma_{HMT(hi-spd)}} = \frac{4.823}{6.202 \times 0.83} = 0.937 \tag{4.11}$$

b. Input-coupled HMT

Determining GR1 and GR2 gear ratios for the input-coupled HMT requires a different approach compared to that for the output-coupled configuration. In input-coupled HMT, the PM 1 is mechanically coupled to the engine via the speed reducer GR1. Thus, to allow both the

engine and PM 1 to operate at full speed range, the GR1 gear ratio is determined by dividing

maximum engine speed by the pump/motor 1 maximum speed (eq. 4.12).

$$\gamma_{GR1-IC} = \frac{\omega_{e(max)}}{\omega_{PM1(max)}} = \frac{219.911}{282.7} = 0.778 \tag{4.12}$$

The GR2 speed reducer gear ratio for input-coupled HMT is calculated by using the definition of

the high-speed equivalent gear ratio (eq. 4.13). Its gear ratio ($\gamma_{eq(hi-spd)}$ =4.823), along with

other ratios needed in eq. 4.13, are known ($\gamma_{HMT(hi-spd.)} = 0.83$ and $\gamma_{GR1} = 0.778$). Thus, GR2

gear ratio can be calculated (eq. 4.14).

$$\gamma_{eq(hi-spd.)} = \gamma_{GR1} \, \gamma_{HMT(hi-spd.)} \, \gamma_{GR2} = 4.823 \tag{4.13}$$

$$\gamma_{GR2-IC} = \frac{4.823}{0.778 \times 0.83} = 7.472 \tag{4.14}$$

This chapter shows the maximum speed of the bus is derived from the maximum

available engine power and is used to find the equivalent gear ratios for both high-speed and

high-torque cases. Both of the equivalent ratios, as well as the physical limitations of the

components, are used to obtain the speed reducers gear ratios (γ_{GR1} and γ_{GR2}) for input- and

output-coupled HMTs. The summary of findings from this chapter is shown in table 4.3

Table 4.3. Speed reducers gear ratios for both input and output coupled HMTs

Input-coupled configuration speed reducers	Gear ratio	Output-coupled configuration speed reducers	Gear ratio
γ_{GR1-IC}	0.778	γ_{GR1-OC}	0.937
γ_{GR2-IC}	7.472	γ_{GR2-OC}	6.202

Chapter 5

HMT configurations and operating modes

This chapter focuses on possible HMT configurations and how they are different from each other. A single-staged HMT consists of two hydraulic PM, one PGS, and a fixed gear coupling. The two hydraulic PM's are labeled PM1, located near the input shaft; and PM2, located near the output shaft.

The single-staged HMT can be divided into two coupling categories: input- and output-coupled, with six possible configurations for each. The input-coupled HMT places fixed gear coupling at the input shaft (hence the name" input-coupled") and a planetary gear at the output shaft (fig. 5.1). The output-coupled HMT places fixed gear coupling at the output shaft and a planetary gear set at the input shaft (fig. 5.2). The twelve HMT configurations are classified according to how each member of the planetary gear set (i.e. sun, carrier, and ring gears) is connected. Another type of HMT is the dual-staged, where planetary gear sets are placed at both the input and the output shafts and has 1,152 possible configurations [24].

5.1 Single-staged HMT classifications.

a. Input-coupled HMT

An input-coupled HMT configuration splits the input power via a fixed gear coupler and re-combined the power back via a planetary gear set (PGS) at the final drive shaft. The PGS consists of three gears, namely, sun, carrier and ring. There are six different ways to connect the

gears into the input coupled HMT and thus there are six possible configurations for the input-coupled HMT.

The six configurations are classified using the three-letter nomenclature convention suggested by Sung (2005) [36]. The HMT name starts with the letter 'I', indicating that the HMT is input-coupled. The second letter denotes which planetary gear is connected to the hydraulic unit, and the third letter denotes which planetary gear is connected the final drive shaft. For instance, an 'IRC' configuration is the input-coupled HMT where the ring gear, 'R', is connected to the hydraulic unit, and the carrier gear, 'C', of the planetary gear set is connected to the transmission's output shaft. Using the same convention, all six input-coupled configurations' names and figures can be determined (table 5.1).

Table 5.1: Configuration nomenclatures of planetary input-coupled HMT and how they are connected

Name	PM2	Output shaft	Mechanical shaft	Figure
IRC	Ring	Carrier	Sun	
ICR	Carrier	Ring	Sun	

ISR	Sun	Ring	Carrier	
IRS	Ring	Sun	Carrier	
ICS	Carrier	Sun	Ring	
ISC	Sun	Carrier	Ring	

b. Output-coupled HMT

An output-coupled HMT splits the input power into the mechanical and the hydraulic power paths via a PGS and re-combines the split power via a fixed gear coupler (fig. 5.2). Like the input-coupled HMT, the output-coupled HMT has also six possible configurations.
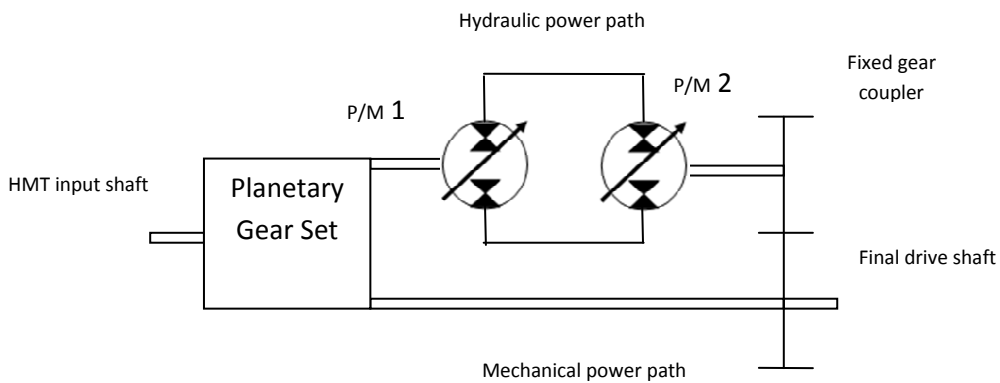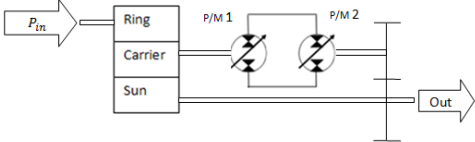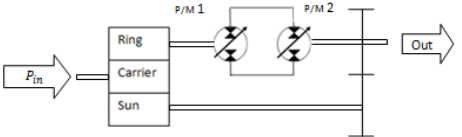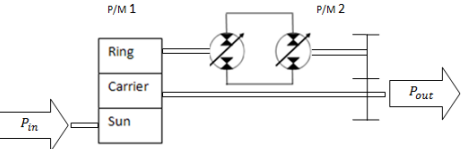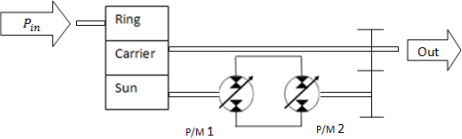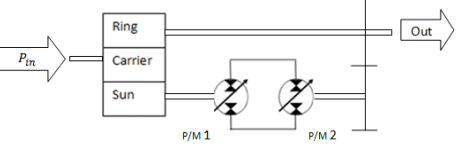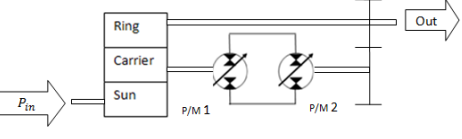
Figure 5.2. General output-coupled HMT drive train structure

Another three-letter nomenclature convention is used to classify the output coupled HMT configurations. The first letter stands for the gear connected to the input shaft, the second letter stands for the gear connected to the hydraulic power branch and the last letter 'O' indicates that the HMT is classified as output-coupled. For example, the 'RSO' HMT is an output-

coupled HMT with the ring gear 'R' connected to the input shaft and the sun gear 'S' connected to the hydraulic unit. Table 5.2 lists the names and the figures of all six output-coupled HMT configurations and their gear connections.

Table 5.2: configurations nomenclatures of planetary output-coupled HMT and how they are connected

Name	Hydraulic power path	Output shaft	Mechanical power path	Figure
RCO	Carrier	Ring	Sun	
CRO	Ring	Carrier	Sun	
SRO	Ring	Sun	Carrier	
RSO	Sun	Ring	Carrier	
CSO	Sun	Carrier	Ring	
SCO	Carrier	Sun	Ring	

Each configuration shown has its own way of managing the input power in the hydraulic and the mechanical power paths. These power management methods are classified in the HMT modes that often changes along the range of HMT speed ratios.

5.2 HMT modes

An HMT can operate in five modes; normal power-split, hydrostatic, mechanical, hydraulic power re-circulation (HPR), and mechanical power re-circulation (MPR). These modes establish how the input power is managed and can be determined by the hydraulic power ratio (P_h) (eq. 5.1). Another ratio worth noting is the mechanical power ratio (eq. 5.2).

$$P_h = \frac{\text{hydraulic power}}{\text{engine power}} \qquad\qquad (5.1)$$

$$P_m = 1 - P_h \qquad\qquad (5.2)$$

P_h is the proportion of the input power in the hydraulic power path. P_m is the proportion of the input power in the mechanical power path (eq. 5.2). Sub sections below (a - e) explain the modes in greater detail with examples in figs. 5.3-5.7, assuming mechanical and hydraulic power path efficiencies of 95% and 60%, respectively. The fixed coupling gear and the planetary gears are assumed to be 100% efficient.

a. Normal power-split mode ($0 < P_h < 1.0$ & $0 < P_m < 1$)

In the normal power-split mode, the engine power is split into the hydraulic and the mechanical power paths, which are then recombined at the output shaft (fig. 5.3). Both the hydraulic and the mechanical power ratios are positive, indicating power being transmitted in the normal direction, where PM1 operates as a pump and PM2 as a motor. This mode is desirable because it allows engine control flexibility and has the benefit of a high-efficiency mechanical transmission. The transmission efficiency during the normal power-split mode varies, according to the P_h value (eq. 5.3). Table 5.3 shows transmission efficiency during the

normal HMT mode ranging higher than hydrostatic and lower than mechanical modes ($\eta_{hyd.} < \eta_{transmission} < \eta_{mech.}$).
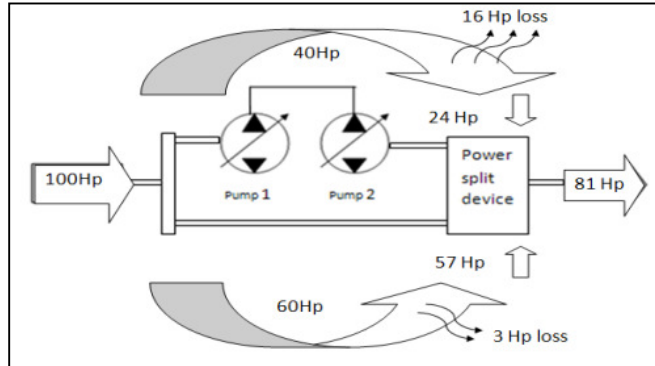
Figure 5.3. Normal HMT mode, when $P_h = 0.6$

$$P_{out} = ((P_h)\eta_{hyd.} + \eta_{mech.}(P_m)) P_{in} , \qquad 0 < P_h < 1 \qquad (5.3)$$

$$\eta_{transmission} = \frac{P_{out}}{P_{in}} = ((P_h)\eta_{hyd.} + \eta_{mech.}(1 - P_h))$$

b. Mechanical mode ($P_h = 0$ & $P_m = 1$)

The mechanical mode occurs when the P_h value is zero and the mechanical power ratio is 1.0, meaning all of the engine power is transferred via the mechanical path. This is the most efficient way of transmitting the power from the engine to the output shaft. However, the engine speed is limited by the output speed and this can be bad for overall efficiency. In the example shown in fig. 5.4, 95% of the input power is transferred to the final drive. In this mode, the transmission efficiency is a constant and the same as the efficiency of the mechanical power path ($\eta_{transmission} = \eta_{mech.}$).
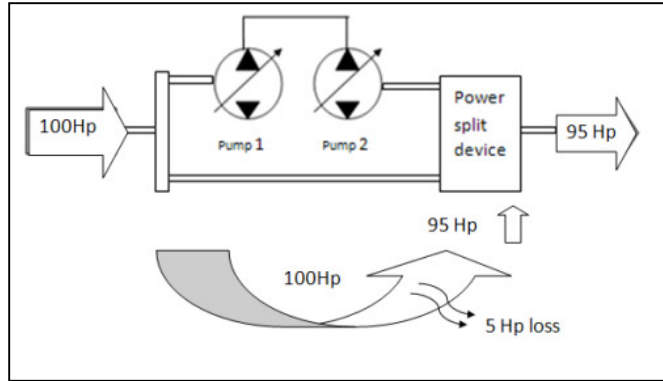
Figure 5.4. Mechanical mode, when $P_h = 0$

c. Hydrostatic mode ($P_h = 1$ & $P_m = 0$)

This mode occurs when all of the engine power goes to the hydraulic power path and the transmission operates as a hydrostatic CVT. Although it allows full engine control, this mode is very sensitive to the PM efficiency. In the example shown in (fig. 5.5), 60% of the engine input power is transferred to the final drive. In this mode, the transmission efficiency is a constant and the same as the efficiency of the hydraulic power path ($\eta_{transmission} = \eta_{hyd.}$).
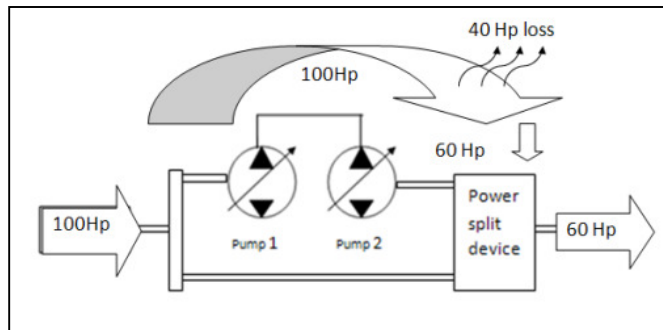
Figure 5.5. Hydrostatic mode, when $P_h = 1.0$

d. MPR ($P_h > 1.0$ & $P_m < 0$)

In the MPR mode, the mechanical power path is reversed (hence the name, "mechanical power recirculation mode"), resulting in high power flow in the hydraulic power path (fig. 5.6). A P_h value larger than 1.0 indicates the power fed into the hydraulic power path is larger than the

engine input. This mode is very inefficient because a large amount of power is transmitted via the inefficient hydraulic power path. The transmission efficiency during the MPR mode is governed by eq. 5.4. Table 5.3 suggests the transmission efficiency during MPR mode is always lower than the hydrostatic mode ($\eta_{transmission} < \eta_{hyd.}$) and this mode should be avoided by transmission design.
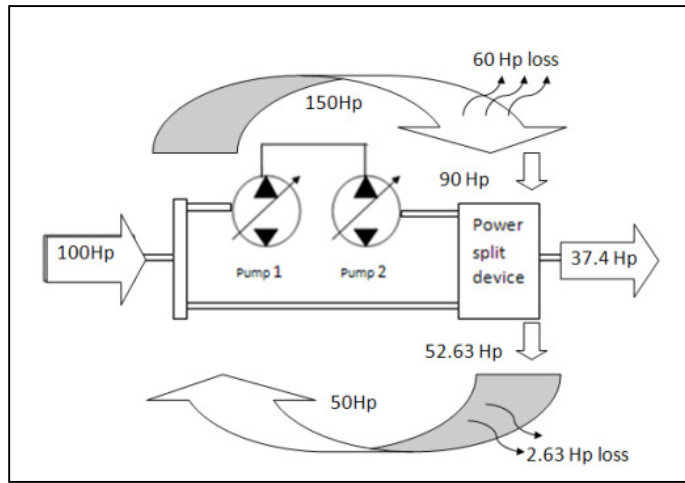
Figure 5.6. MPR mode, when $P_h = 1.5$

$$P_{out} = ((P_{in} + (P_h - 1)P_{in})\eta_{mech.})\eta_{hyd.} - P_{in}(P_h - 1), \qquad P_h > 1.0 \qquad (5.4)$$

$$\eta_{transmission} = \frac{P_{out}}{P_{in}} = ((1 + (P_h - 1))\eta_{mech.})\eta_{hyd.} - (P_h - 1)$$

  e. HPR ($P_h < 0$ & $P_m > 1$)

In the HPR mode, the hydraulic power path is reversed as PM2 operates as a pump and PM1 operates as a motor (Fig. 5.7). A negative P_h value indicates reversed hydraulic power (hence the name, "hydraulic power recirculation mode"), which results in high power flow in the mechanical power path. The mode is usable, up to a certain degree, because most of the power is transmitted through a high efficient mechanical power path. The equation of the transmission efficiency during the HPR mode is derived (eq. 5.5) and is used in table 5.3 to show the transmission efficiency response to P_h values. The lower the P_h value, the more power is re-

circulated and thus lowers the transmission efficiency. Table 5.3 suggests, mild HPR mode (P_h value near zero) is more efficient than the hydrostatic mode.

$$P_{out} = ((P_{in} + abs(P_h)P_{in})\eta_{hyd.})\eta_{mech.} - P_{in}abs(P_h), \qquad P_h < 0 \qquad (5.5)$$

$$\eta_{transmission} = \frac{P_{out}}{P_{in}} = ((1 + abs(P_h))\eta_{hyd.})\eta_{mech.} - abs(P_h)$$
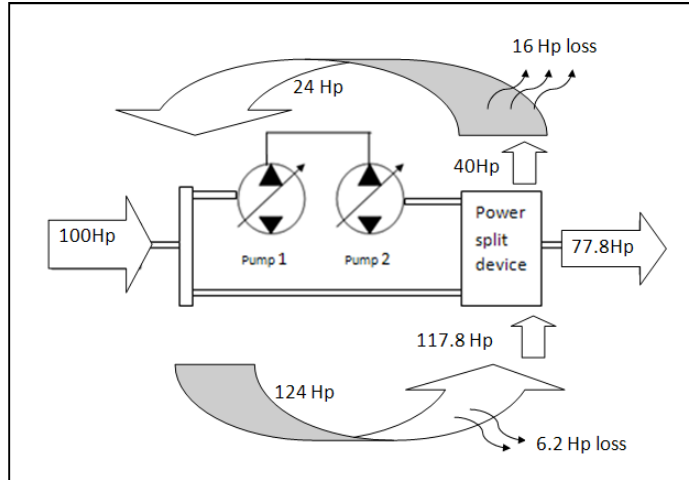
Figure 5.7 HPR mode, when $P_h = -0.4$

The subsections show that the HPR, the normal HMT- split, and the MPR modes have ranges of transmission efficiencies depending on P_h values. The efficiency ranges are calculated using eqs. 5.3 - 5.5 based on P_h values (table 5.3). From the calculations, it can be seen the low efficient MPR mode should be avoided by design and HPR mode can be used, up to certain degree. The usable range of HPR mode is called 'mild HPR' and its transmission efficiency is comparable to the normal power-split mode.

Table 5.3. Transmission efficiency in different modes

P_h (Normal mode)	η_{trans} (%)	P_h (MPR mode)	η_{trans} (%)	P_h (HPR mode)	η_{trans} (%)
0	95	1.0	60	0	95
0.10	91.5	1.10	55.7	-0.10	90.7
0.20	88	1.20	51.4	-0.20	86.4

0.30	84.5	1.30	47.1	-0.30	82.1
0.40	81	1.40	42.8	-0.40	77.8
0.50	77.5	1.50	38.5	-0.50	73.5
0.60	74	1.60	34.2	-0.60	69.2
0.70	70.5	1.70	29.9	-0.70	64.9
0.80	67	1.80	25.6	-0.80	60.6
0.90	63.5	1.90	21.3	-0.90	56.3
1.00	60	1.100	17	-1.00	52

5.3 P_h vs. speed ratio derivations and plot

The HMT operating mode changes, depending on its speed ratio. Its changing pattern can be viewed using the P_h vs. the speed ratio plot. Fig. 5.8 shows an example of how the HMT operating mode changes from HPR to mechanical and finally to normal HMT as speed ratio goes from 0 to 1.25.
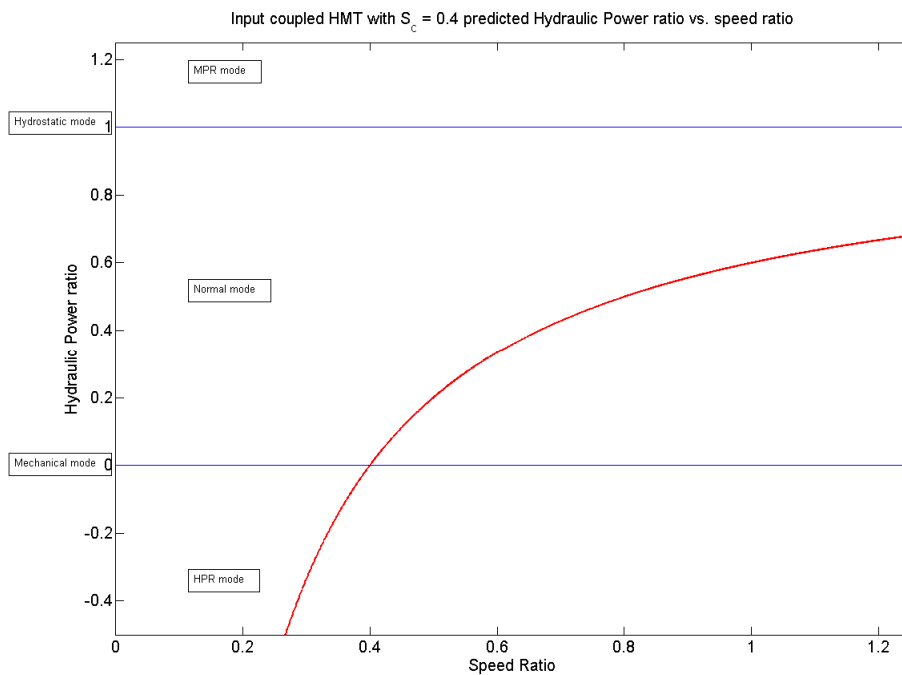
Figure 5.8. Typical hydraulic power ratio vs. speed ratio plot

35

In this study, P_h values are derived in terms of speed ratios for all twelve configurations. The IRC configuration is used as an example to derive the input-coupled HMT P_h equation (section 5.3.1), while the RSO is used for the output-coupled HMT (section 5.3.2). The equation derivation assumes there is no hydraulic accumulator and 100% efficiency transmission, resulting in equal power in PM1 or PM2 (eq. 5.6) and equal input and output power (eq. 5.7).

$$P_{\text{hydraulic}} = T_{\text{hyd}}\,\omega_{\text{hyd}} = T_{\text{PM1}}\omega_{\text{PM1}} = T_{\text{PM2}}\omega_{\text{PM2}} \qquad (5.6)$$

$$P_h = \frac{P_{\text{hydraulic}}}{P_{\text{input}}} = \frac{P_{\text{hydraulic}}}{P_{\text{output}}} \qquad (5.7)$$

5.3.1. Input-coupled HMT kinematic equation: the IRC case derivation

The IRC is an input-coupled HMT with the ring gear is connected to PM2, the sun gear to the mechanical drive shaft and the carrier gear to the output shaft (fig. 5.9). Thus, the speed and the torque (neglecting the dynamics) are simplified as follows:
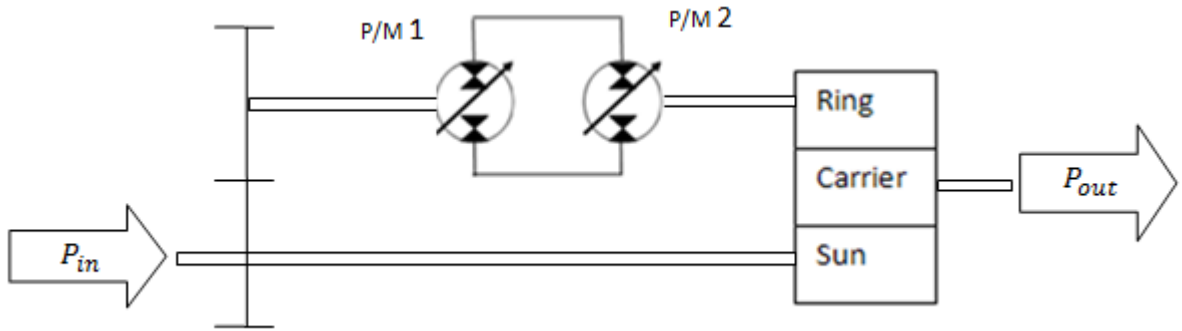
Figure 5.9: IRC input-coupled HMT configuration

$$\omega_{\text{in}} = \omega_{\text{sun}} \qquad\qquad \omega_{\text{PM2}} = \omega_{\text{ring}} \qquad\qquad \omega_{\text{out}} = \omega_{\text{carrier}}$$

And

$$T_{\text{in}} = T_{\text{sun}} + T_{\text{PM1}} \qquad\qquad T_{\text{PM2}} = T_{\text{ring}} \qquad\qquad T_{\text{out}} = T_{\text{carrier}}$$

The PGS speed is governed by the planetary gears' speed equation (eq. 5.8) and the torque of the IRC drive train is determined by the torque lever diagram (fig. 5.10).

$$\omega_{\text{ring}} R + \omega_{\text{sun}} S = \omega_{\text{carrier}} (R + S) \tag{5.8}$$

$$\omega_{\text{PM2}} = \omega_{\text{ring}} = \omega_{\text{carrier}} \left(\frac{R+S}{R}\right) - \frac{\omega_{\text{sun}} S}{R} = \frac{\omega_{\text{out}}(R+S) - \omega_{\text{input}} S}{R} \tag{5.9}$$
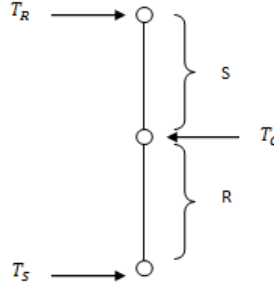
Figure 5.10. IRC torque diagram

The torque diagram is treated like a moment equilibrium problem to derive the torque equation. The derivation also neglects the system dynamics and only takes into account the system kinematics. From the moment equilibrium equation, the equation of pump/motor 2, T_{PM2}, in terms of output shaft torque, T_{out}, is derived (eq. 5.10).

$$T_R(S + R) = T_C R$$

$$T_{\text{PM2}} = T_{\text{out}} \frac{R}{S+R} \tag{5.10}$$

With the torque and speed of PM2 defined, the hydraulic power ratio equation is written as in eq. 5.11

$$P_h = \frac{P_{\text{hydraulic}}}{P_{\text{output}}} = \frac{\tau_{\text{PM2}} * \omega_{\text{PM2}}}{\tau_{\text{out}} * \omega_{\text{out}}} = \frac{\frac{T_{\text{out}} R}{(R+S)} \frac{\omega_{\text{out}}(R+S) - \omega_{\text{input}} S}{R}}{T_{\text{FD}} \omega_{\text{out}}} = 1 - \frac{1}{1+h} \left(\frac{1}{\omega_{\text{rat}}}\right) \tag{5.11}$$

The same process is repeated for the rest of the six input-coupled HMT configurations (table 5.4). They all use the same planetary speed equation (eq. 5.8), but different torque equations, depending on the torque lever diagram. The torque equations used for all input coupled configurations are described in the fourth column of table 5.4.

5.3.2 Output-coupled HMT kinematic equation: the SRO case derivation

For the output-coupled HMT, the SRO configuration is used as an example. The sun gear is connected to the input shaft, the ring gear to PM1 and the carrier gear to the mechanical drive shaft (fig. 5.11). Like the input-coupled, the drive train is studied neglecting the dynamics, and focuses on the kinematics.

Table 5.4: All six input-coupled HMT configurations with P_h equations

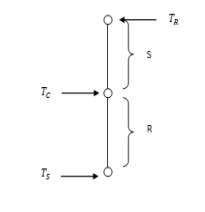| Conf.	Hydraulic speed	Torque lever	Hydraulic torque	P_h equations
IRC	ω_{ring} $= \dfrac{(\omega_{carrier}\,(R+S) - \omega_{sun}\,S)}{R}$	$T_R \rightarrow$ … T_c … $T_s \rightarrow$	$T_{Ring} = \dfrac{T_{Carrier}\,R}{(S+R)}$	P_h $= 1$ $- \dfrac{1}{1+h}\left(\dfrac{1}{\omega_{rat}}\right)$
ISR	ω_{sun} $= \dfrac{(\omega_{carrier}\,(R+S) - \omega_{ring}\,R)}{S}$	T_R … $T_c \rightarrow$ … $T_s \rightarrow$	$T_{Sun} = -\dfrac{T_{Ring}\,S}{R}$	P_h $= 1$ $- \dfrac{1+h}{h}\left(\dfrac{1}{\omega_{rat}}\right)$
IRS	ω_{ring} $= \dfrac{(\omega_{carrier}\,(R+S) - \omega_{sun}\,S)}{R}$	$T_R \rightarrow$ … $T_c \rightarrow$ … T_s	$T_{Ring} = -\dfrac{T_{Sun}\,R}{S}$	P_h $= 1 - (1$ $+ h)\left(\dfrac{1}{\omega_{rat}}\right)$
ICS	$\omega_{carrier} = \dfrac{(\omega_{sun}\,S + \omega_{ring}\,R)}{(R+S)}$	$T_R \rightarrow$ … $T_c \rightarrow$ … T_s	$T_{Carrier}$ $= \dfrac{T_{Sun}\,(R+S)}{S}$	$P_h = 1 + h\left(\dfrac{1}{\omega_{rat}}\right)$
ISC	ω_{sun} $= \dfrac{(\omega_{carrier}\,(R+S) - \omega_{ring}\,R)}{S}$	$T_R \rightarrow$ … T_c … $T_s \rightarrow$	$T_{Sun} = \dfrac{T_{Carrier}\,S}{(S+R)}$	P_h $= 1$ $- \dfrac{h}{1+h}\left(\dfrac{1}{\omega_{rat}}\right)$

ICR	$\omega_{carrier} = \dfrac{(\omega_{sun} S + \omega_{ring} R)}{(R + S)}$		$T_{Carrier}$ $= \dfrac{T_{Ring}(S + R)}{S}$	$P_h = 1 + \dfrac{1}{h}\left(\dfrac{1}{\omega_{rat}}\right)$

$$\omega_{in} = \omega_{sun} \qquad\qquad \omega_{PM1} = \omega_{ring} \qquad \omega_{mech} = \omega_{out} = \omega_{carrier}$$

And

$$T_{in} = T_{sun} \qquad\qquad T_{PM1} = T_{ring} \qquad T_{mech} = T_{carrier}$$
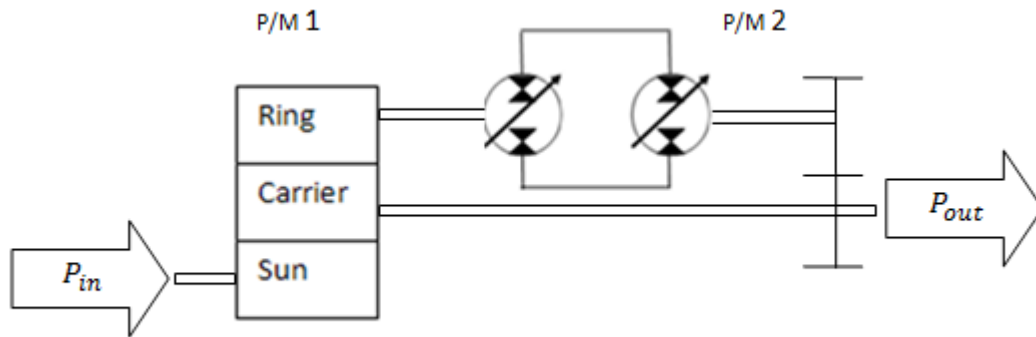
Figure 5.11. SRO output-coupled HMT configuration

The P_h equation in this case is the ratio of the powers at the ring gear to the input power (eq. 5.12). The ring gear speed equation (eq.5.13) is derived from the PGS eq. (5.8).

$$P_h = \frac{P_{hydraulic}}{P_{in}} = \frac{T_{ring}\omega_{ring}}{T_{in}\omega_{in}} \qquad\qquad (5.12)$$

$$\omega_{ring} = \frac{(\omega_{carrier}\,(R+S) - \omega_{sun}\,S)}{R} = \frac{(\omega_{out}\,(R+S) - \omega_{in}\,S)}{R} \qquad\qquad (5.13)$$

Like in the case of input coupled HMT, the PGS torque is governed by an equation based on the torque lever diagram (fig. 5.12).
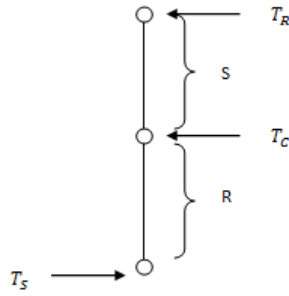
Figure 5.12. SRO torque diagram

$$T_R S = -T_S R$$

$$T_{PM1} = -T_{in} \frac{R}{S} \qquad (5.14)$$

With the torque and speed of PM1 defined, the hydraulic power ratio equation is derived (eq.

5.15). The same process is repeated for the rest of the six configurations (table 5.5).

$$P_h = \frac{T_{ring}\,\omega_{ring}}{T_{in}\omega_{in}} = -\frac{T_{in}\,R(\,\omega_{out}\,(R+S)-\,\omega_{in}\,S)}{R\,S\,T_{in}\omega_{in}} = 1 - (h+1)\omega_{rat} \qquad (5.15)$$

Table 5.5: All six output-coupled HMT configurations with P_h equations

Conf.	Hydraulic speed	Torque lever	Hydraulic Torque	P_h equations
RCO	$\omega_{carrier} = \dfrac{(\omega_{sun}\,S + \omega_{ring}\,R)}{(R+S)}$		$T_{carrier} = \dfrac{T_{ring}\,(S+R)}{R}$	$P_h = 1 + \dfrac{\omega_{rat}}{h}$
CRO	$\omega_{ring} = \dfrac{(\omega_{carrier}\,(R+S) - \omega_{sun}\,S)}{R}$		$T_{ring} = \dfrac{T_{carrier}\,R}{S+R}$	$P_h = 1 - \dfrac{\omega_{rat}}{h+1}$

SRO	ω_{ring} $= \dfrac{(\omega_{carrier}\,(R+S) - \omega_{sun}\,S)}{R}$		$T_{Ring} = -\dfrac{T_{Sun}\,R}{S}$	P_h $= 1 - (1$ $+ h)\omega_{rat}$
RSO	ω_{sun} $= \dfrac{(\omega_{carrier}\,(R+S) - \omega_{ring}\,R)}{S}$		$T_{sun}R = \dfrac{-T_{ring}\,S}{R}$	P_h $= 1$ $-\dfrac{1+h}{h}\omega_{rat}$
CSO	ω_{sun} $= \dfrac{(\omega_{carrier}\,(R+S) - \omega_{ring}\,R)}{S}$		$T_{Sun} = \dfrac{T_{Carrier}\,S}{(S+R)}$	P_h $= 1$ $-\dfrac{h}{h+1}\omega_{rat}$
SCO	$\omega_{carrier} = \dfrac{(\omega_{sun}\,S + \omega_{ring}\,R)}{(R+S)}$		$T_{Carrier}$ $= \dfrac{T_{sun}\,(S+R)}{S}$	P_h $= 1 + h\,\omega_{rat}$

5.3.3 P_h vs speed ratio plot

The P_h equations for all twelve configurations derived (table 5.4 & 5.5) are plotted in table 5.6, assuming they use same planetary gear ratio, h =2. In general, the input-coupled configurations show a nonlinear P_h response to the speed ratio, while the output-coupled configurations show a linear response. The plots show the P_h values, which then describe the HMT modes, along the speed ratio range from zero to one. Of all the single-staged HMT configurations, ICR, ICS, RCO, and SCO can potentially operate in the low-efficiency MPR mode. Thus, these configurations are eliminated.

I.C.	P_h vs speed ratio plot (h =2)	O.C.	P_h vs speed ratio plot (h =2)
IRC		RCO	
ISR		CRO	
IRS		SRO	
ICS		RSO	

ISC	Hydraulic power ratio vs Speed ratio (ISC)	CSO	Hydraulic power ratio vs Speed ratio (CSO)
ICR	Hydraulic power ratio vs Speed ratio (ICR)	SCO	Hydraulic power ratio vs Speed ratio (SCO)
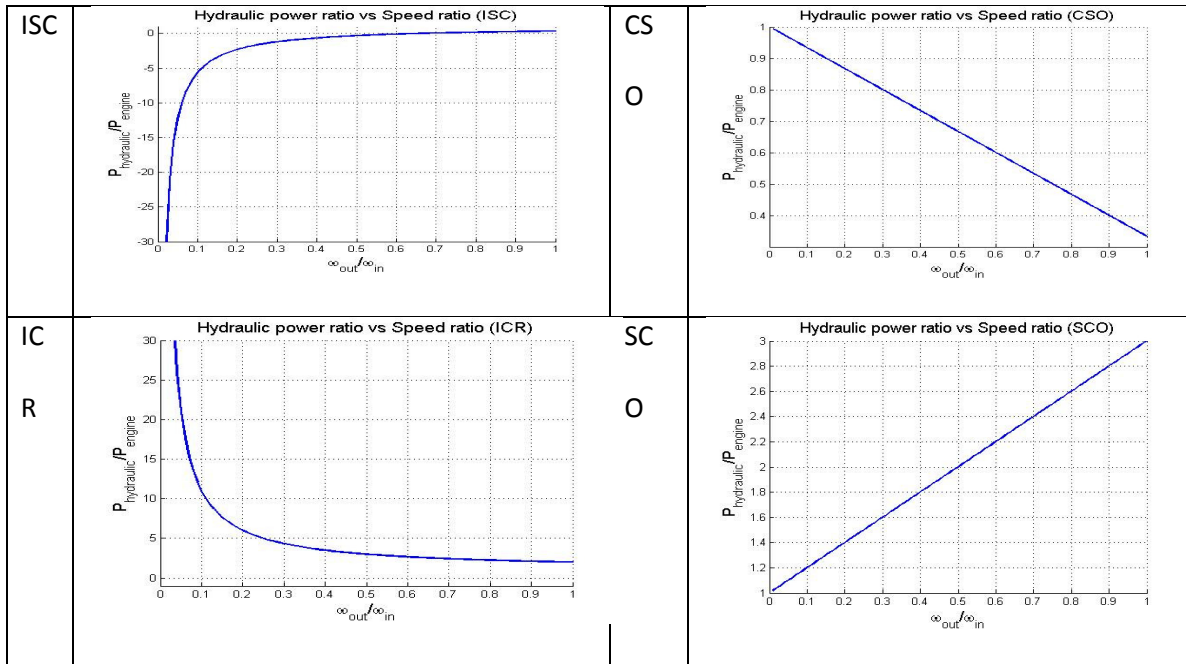
This chapter shows the unique behaviors of all twelve single-staged HMT configurations along the speed ratio range. Thus, it is possible to find the optimal HMT configuration for a city bus among these twelve candidates. However, this exhaustive search can be very time consuming, especially if the study ventures to search the 1,152 possible dual-staged HMT candidates. In the following chapters, the optimization task is simplified by using the critical speed ratio.

Chapter 6

HMT configuration generalization and candidates

The nomenclature convention from the previous chapter describes how the PGS is connected in the HMT. The convention, however, does not describe configuration's behavior along the speed ratio range. Thus, finding an optimal configuration among the twelve configurations is a time-consuming process. In this chapter, the generalized P_h equation that can pin-point a specific configuration is introduced. This makes the configuration optimization process much simpler.

6.1 Critical speed ratio

The previous chapter shows the input-coupled HMT generally has a nonlinear hydraulic power ratio (P_h) response to the speed ratio while the output-coupled HMT shows a linear response. The plots in table 5.6 show different configurations (from the same coupling category) are differentiated by the point when the configuration changes its mode from normal to hydraulic power re-circulation (HPR) or vice versa. This particular point is introduced in this research as the critical speed ratio (S_{crit}). It is the speed ratio when an HMT drive train operates at the mechanical mode $(P_h = 0)$. Thus, naming a specific HMT configuration can be reduced to specifying coupling type and S_{crit} value. For example, an input-coupled HMT with the S_{crit} 0.4 would mean a nonlinear P_h response to speed ratio (ω_{rat}) with the x- intercept at $S_{crit} = 0.4$ (fig. 6.1). From the $P_h\ vs.\ \omega_{rat}$ plot, the configuration's mode change along the speed ratio range can be determined (table 6.1).

Modes	Speed ratio (ω_{rat})
HPR	$0 < \omega_{rat} < S_{crit}$
Mechanical	$\omega_{rat} = S_{crit}$
Normal power split	$S_{crit} < \omega_{rat} < \infty$

Input coupled HMT with S_c = 0.4 predicted Hydraulic Power ratio vs. speed ratio
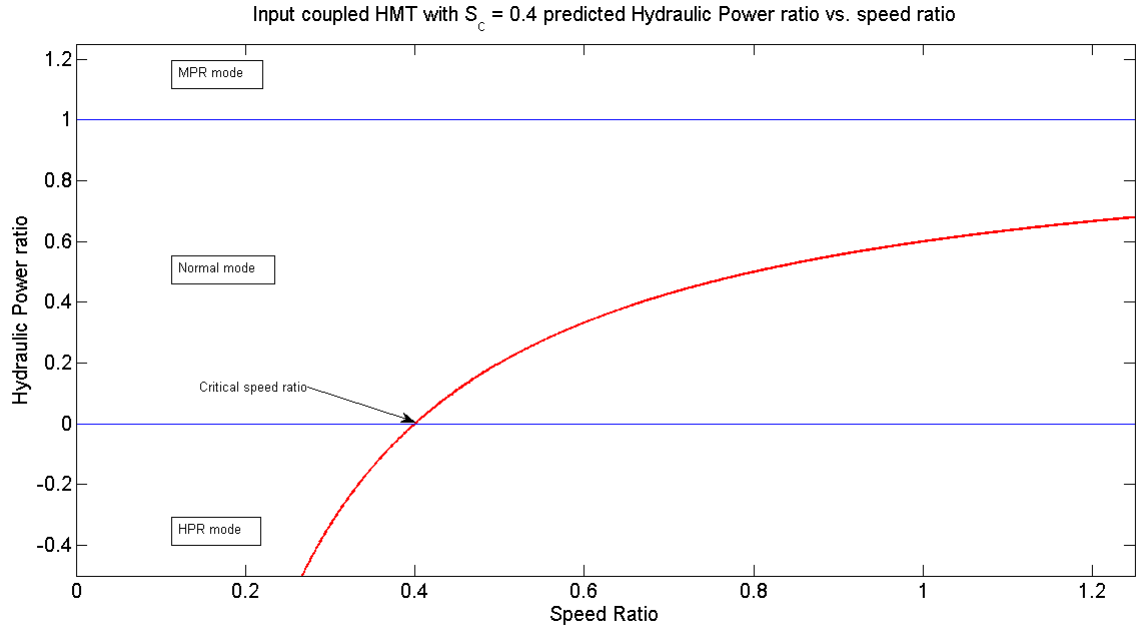
Figure 6.1. P_h vs. ω_{rat} plot for input-coupled HMT with S_{crit} 0.4

Another example is an output-coupled HMT with $S_{crit} = 0.4$. The $P_h \ vs. \ \omega_{rat}$ plot for the output-coupled configuration intercepts the y-axis at P_h =1, and decreases linearly with respect to the speed ratio with and intercepts the x-axis at S_{crit} = 0.4 (fig. 6.2). The configuration's mode change throughout the speed ratio range is shown in table 6.2. These two short examples show that any single staged HMT configuration can be specified by its coupling type (input or output coupled) and its S_{crit} value.

Modes	Speed ratio (ω_{rat})
Hydrostatic	$\omega_{rat} = 0$
Normal power split	$0 < \omega_{rat} < S_{crit}$
Mechanical	$\omega_{rat} = S_{crit}$
HPR	$S_{crit} < \omega_{rat} < \infty$
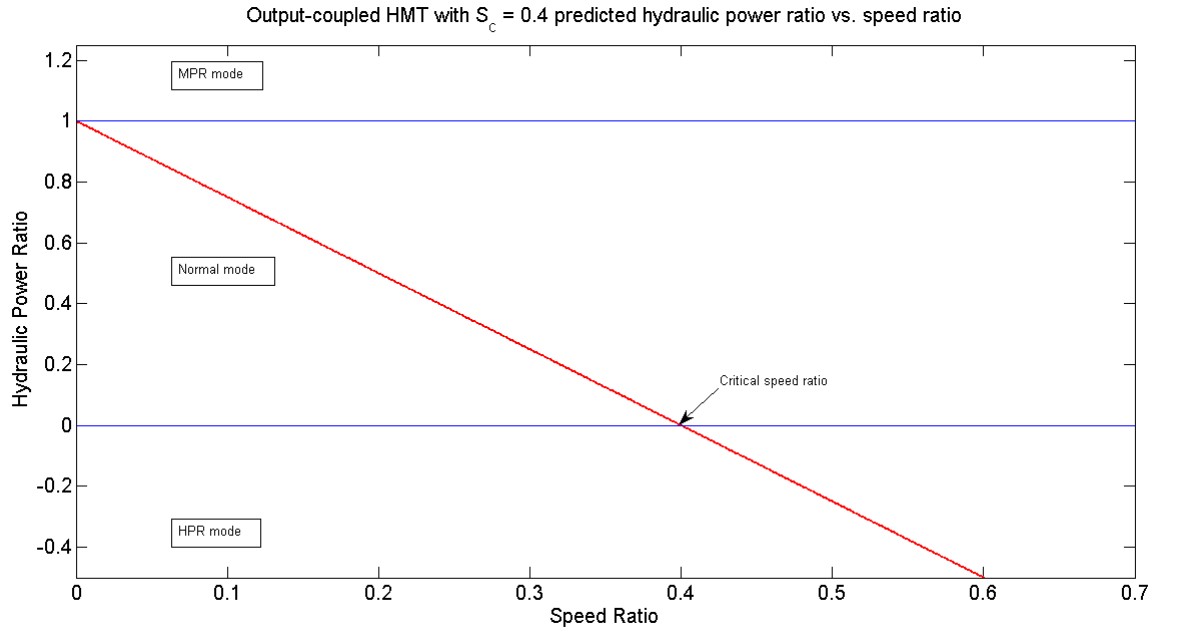
Figure 6.2. P_h vs. ω_{rat} plot for output-coupled HMT with S_{crit} 0.4

6.2 Generalized HMT and S_{crit} equations

The P_h equations for the twelve HMT configurations can be generalized into two, one for each coupling type (eqs. 6.1 and 6.2). A generalized P_h equation for each coupling type is used to determine the S_{crit} equations for the twelve configurations by comparing the generalized equations to the P_h equations obtained from the previous chapter (table 6.3).

$$P_{h(OC)} = 1 - \frac{1}{S_{crit}} * \omega_{rat} \qquad\qquad (6.1)$$

$$P_{h(IC)} = 1 - S_{crit} * \frac{1}{\omega_{rat}} \qquad\qquad (6.2)$$

Table 6.3. The twelve HMT configurations with their P_h and S_{crit} equations

Input-coupled	P_h equations	S_{crit}	Output-coupled	P_h equations	S_{crit}
IRC	$1 - \dfrac{1}{1+h}\left(\dfrac{1}{\omega_{rat}}\right)$	$\dfrac{1}{1+h}$	RCO	$1 + \dfrac{\omega_{rat}}{h}$	$-h$
ISR	$1 - \dfrac{1+h}{h}\left(\dfrac{1}{\omega_{rat}}\right)$	$\dfrac{1+h}{h}$	CRO	$1 - \dfrac{\omega_{rat}}{h+1}$	$h+1$
IRS	$1 - (1+h)\left(\dfrac{1}{\omega_{rat}}\right)$	$1+h$	SRO	$1 - (1+h)\omega_{rat}$	$\dfrac{1}{h+1}$
ICS	$1 + h\left(\dfrac{1}{\omega_{rat}}\right)$	$-h$	RSO	$1 - \dfrac{1+h}{h}\omega_{rat}$	$\dfrac{h}{h+1}$
ISC	$1 - \dfrac{h}{1+h}\left(\dfrac{1}{\omega_{rat}}\right)$	$\dfrac{h}{1+h}$	CSO	$1 - \dfrac{h}{h+1}\omega_{rat}$	$\dfrac{h+1}{h}$
ICR	$1 + \dfrac{1}{h}\left(\dfrac{1}{\omega_{rat}}\right)$	$-\dfrac{1}{h}$	SCO	$1 + h\,\omega_{rat}$	$-\dfrac{1}{h}$

Theoretically, with this generalization, any of the six configurations (from the same coupling type) can become any other equivalent physical configuration by manipulating the *h* value. For example, IRC configuration with planetary gear ratio h = 7/3 is kinematically the same as the ISC configuration with planetary gear ratio h = 3/7. Both of these physical configurations are the equivalent to the input coupled HMT with $S_{crit} = 0.4$. In PGS design, however, the ring gear must be bigger than the sun. Thus, the planetary gear ratio '$h = \dfrac{R}{S}$' to be greater than 1 (*h>1)* is defined as a physical constraint in HMT design. This mean, from the example, ISC configuration with planetary gear ratio h = 3/7 cannot physically exist. Because of this PGS physical constraint, a configuration with a specified coupling type and S_{crit} value can only exist in the form of one physical HMT configuration. For example, an input-coupled HMT with S_{crit} =0.1 can only exist in the IRC configuration. Table 6.4 shows the generalized HMT configurations with their matching physical configurations. S_{crit}= 0.5 is excluded from the candidate list because the HMT with such S_{crit} value would result in the h value of less than 1, which is physically nonexistent.

Table 6.4. The planetary gear ratio 'h' for different configurations

Input-coupled w. S_{crit}	Configuration	$h = \dfrac{R}{S}$	Output-coupled w. S_{crit}	Configuration	$h = \dfrac{R}{S}$
0.1	IRC	9	0.1	SRO	9
0.2	IRC	4	0.2	SRO	4
0.3	IRC	7/3	0.3	SRO	7/3
0.4	IRC	3/2	0.4	SRO	3/2
0.6	ISC	3/2	0.6	RSO	3/2
0.7	ISC	7/3	0.7	RSO	7/3
0.8	ISC	4	0.8	RSO	4
0.9	ISC	9	0.9	RSO	9

6.3 Optimal HMT design candidates

The fuel efficiency of a vehicle is reflected in the overall drive train efficiency (eq. 6.3). Thus, an optimal configuration should allow both engine and transmission (HMT) to work at their best operating conditions.

$$\eta_{overall} = \eta_{transmission} \times \eta_{engine} \qquad (6.3)$$

Chapter 5 shows that the normal HMT and mild HPR modes are able to achieve better transmission efficiency than the hydrostatic mode and are considered as high efficiency modes. At speed ratio less than the critical, the input coupled HMT operates in HPR mode and shifts to normal mode as the speed ratio becomes larger than the critical (fig. 6.1). Thus, the optimal configuration search process for the input coupled HMT should place the S_{crit} values at low side of the speed ratios range so that the transmission could utilize the high efficient modes. The output coupled, on the other hand, operates at normal HMT mode at speed ratio less than the critical and shifts to HPR mode at speed ratio larger than the critical (fig. 6.2). Thus, for output coupled HMT, the optimal configuration search process should place the S_{crit} values at high side

of the speed ratios range. Based on these characteristics, the input-coupled HMT candidates are assigned with S_{crit} values ranging from 0.28 to 0.52, while the output-coupled HMT candidates are assigned with S_{crit} values ranging from 0.52 to 0.70 (table 6.5).

Table 6.5. Single-staged HMT configuration candidates

Configurations	S_{crit}	h	Configurations	S_{crit}	h
IRC	0.28	72/28	RSO	0.52	52/48
IRC	0.30	7/3	RSO	0.60	6/4
IRC	0.40	2/3	RSO	0.62	62/38
IRC	0.45	45/55	RSO	0.65	65/35
IRC	0.48	48/52	RSO	0.68	68/32
ISC	0.52	52/48	RSO	0.70	7/3

6.4 Dual-staged HMT drive train

Input-coupled HMTs have the tendency to operate in the HPR mode at speed ratios lower than the critical while output-coupled HMTs have the tendency to operate in the HPR mode at speed ratios greater than the critical. The HPR mode can be avoided by utilizing output- and input-coupled HMTs with the same S_{crit} value in one transmission system. This is implemented by using a dual-staged HMT capable of operate as both input- and output-coupled HMTs. The dual-staged HMT operates as output-coupled HMT when the speed ratio is below the critical value, ($\omega_{rat} < S_{crit}$), where only the hydrostatic and the CVT modes are possible. Once the speed ratio exceeds the critical value ($\omega_{rat} \geq S_{crit}$), the dual-staged HMT shifts to the input-coupled mode, where only the mechanical and the normal power-split modes are possible. Fig. 6.3 shows P_h $vs. S_{crit}$ plot for dual staged HMT with S_{crit} 0.4 and table 6.6 shows

49

its modes. Another set of candidate model for dual-staged HMT configurations are used to study
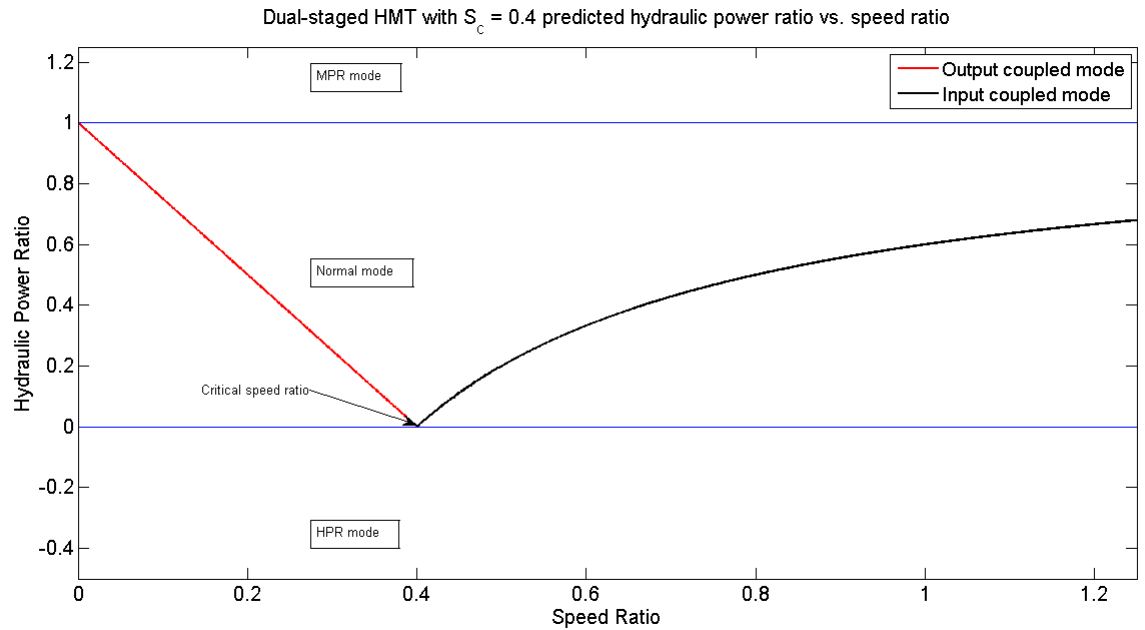
its potential fuel economy (table 6.7).

Figure 6.3. P_h vs. ω_{rat} plot for dual-staged HMT with S_{crit} 0.4

Although theoretically, the dual-staged HMT avoids any power re-circulation, shifting

between the input- and output-coupling modes could cause discontinuity in the drive train

operation and a complex clutch control system is likely needed to ensure smooth operation.

Table 6.6. Change of modes for dual-staged HMT with $S_{crit} = 0.4$

Modes	Speed ratio (ω_{rat})
Hydrostatic	$\omega_{rat} = 0$
Normal power split	$0 < \omega_{rat} < S_{crit}$
Mechanical	$\omega_{rat} = S_{crit}$
Normal power split	$S_{crit} < \omega_{rat} < \infty$

This chapter introduces the critical speed ratio (S_{crit}), a useful tool that allows one to

create a specific HMT configuration and subsequently greatly simplify the search for the HMT

optimal configuration. Twelve single-staged HMT configurations and five dual-staged HMT

configurations are chosen as candidates for optimal simulation in described in the following

chapters.

Table 6.7. Dual-staged HMT configuration candidates

S_{crit}	PGS 1 configuration	PGS 2 configuration
0.4	SRO, $h = \dfrac{3}{2}$	IRC, $h = \dfrac{3}{2}$
0.45	SRO, $h = \dfrac{55}{45}$	IRC, $h = \dfrac{55}{45}$
0.48	SRO, $h = \dfrac{52}{48}$	IRC, $h = \dfrac{52}{48}$
0.52	RSO, $h = \dfrac{52}{48}$	ISC, $h = \dfrac{52}{48}$
0.60	RSO, $h = \dfrac{3}{2}$	ISC, $h = \dfrac{3}{2}$

Chapter 7

Drive train component modeling, simulation and optimal control strategy

The speed reducers' (GR1 and GR2) gear ratios and the HMT configuration candidates were obtained in the parameter study, as described in previous chapters. The study regarded the HMT drive train mainly as a transmission (with no hybrid system included) and only considered the kinematic aspect. In this chapter, the HMT hybrid candidates obtained in parameter study are modeled and simulated with the hybrid energy storage system (hydraulic accumulators) and with the dynamic aspect of the drive train.

7.1 Drive train component modeling

Component modeling is the set of equations or the pre-defined performance map used to represent the components in the simulation. There are three drive train components that are modeled in the simulation; the Hydraulic PM, the high pressure accumulator (HPA), and the diesel engine.

a. Hydraulic pump/motor (PM)

Two swash-plate variable-displacement hydraulic PMs are used in a HMT drive train (table 7.1). PM1, located near the input shaft (fig. 5.1), normally operates as a pump, and PM2, located near the output shaft (fig. 5.1), normally operates as a motor. Since both PMs normally operate as opposite function, their displacement ratio (x) signs are opposite to each other. The

displacement ratio of PM1 (x1) is positive when in pump mode and negative when in motor mode. The opposite convention is applied for displacement ratio of PM2 (x2) (eq. 7.1 – 7.8). The PMs are also subjected to friction loss that is represented by the mechanical efficiency (η_m), and leakage loss that is represented by the volumetric efficiency (η_v). The flow through the PMs $(Q_1 \& Q_2)$ are proportional to the PMs' speed $(\omega_{PM1} \& \omega_{PM2})$, the volumetric efficiency (η_v) and the displacement ratio $(x_1 \& x_2)$ (eqs. 7.1 – 7.4).

$$Q_{x1 \geq 0} = \omega_{PM1} D_1 x_1 \eta_v \qquad \text{Mode: pump} \qquad (7.1)$$

$$Q_{x1 < 0} = \frac{\omega_{PM1} D_1 x_1}{\eta_v} \qquad \text{Mode: motor} \qquad (7.2)$$

$$Q_{x2 < 0} = \omega_{PM2} D_2 x_2 \eta_v \qquad \text{Mode: pump} \qquad (7.3)$$

$$Q_{x2 \geq 0} = \frac{\omega_{PM2} D_2 x_2}{\eta_v} \qquad \text{Mode: motor} \qquad (7.4)$$

The torque produced/absorbed by both PM units is proportional to the system pressure(P), the mechanical efficiency (η_m) and the displacement ratio $(x_1 \& x_2)$ (eqs. 7.5 – 7.8).

$$T_{x1 < 0} = PD_1 x_1 \eta_m \qquad \text{Mode: motor} \qquad (7.5)$$

$$T_{x1 \geq 0} = \frac{PD x_1}{\eta_m} \qquad \text{Mode: pump} \qquad (7.6)$$

$$T_{x2 < 0} = \frac{PD x_2}{\eta_m} \qquad \text{Mode: pump} \qquad (7.7)$$

$$T_{x2 \geq 0} = PD_2 x_2 \eta_m \qquad \text{Mode: motor} \qquad (7.8)$$

Industry-provided swash plate PM efficiency maps are interpolated to obtain mechanical and volumetric efficiencies. The 3D-efficiency maps for motor and pump operations are included in appendices. The hydraulic PM units are modeled with the consideration of their inertia. Thus, their equations of motion are different depending on the modes.

PM motion equation in motor mode:

$$T_{motor} - T_{load} = J_{eq} \dot{\omega}_{PM} \rightarrow PD_1 x_1 \eta_m - T_{load} = J_{eq} \dot{\omega}_{PM} \qquad (7.9)$$

PM motion equation in pump mode:

$$T_{source} - T_{pump} = J_{eq}\dot{\omega}_{PM} \rightarrow T_{source} - \frac{PDx_2}{\eta_m} = J_{eq}\dot{\omega}_{PM} \qquad (7.10)$$

Table 7.1. Specification of hydraulic pump/motor

Brand/ model	Displacement (cc/rev)	Mass	Torque range (Nm)	Speed range (rad/s)	Moment of inertia
Bosch A4VG	250	84.37 kg	-1590 to 1590	-314.2 to 314.2	0.089

b. High-Pressure Accumulator (HPA)

The HPA is an energy storage component that stores potential energy in terms of pressurized hydraulic fluid. The fluid, in this simulation, is assumed to be incompressible that flows into or out of the (HPA) to vary the pressure inside the HPA. In the simulation, the flow of the hydraulic system (sum of flows from both PMs) is equal to the flow in the accumulator (eq. 7.11).

$$Q_{HPA}(t,u) = \frac{\Delta V_{oil,accum.}(t,u)}{\Delta t} = Q_{sys}(t,u) = Q_{PM1}(t,u) + \left(-Q_{PM2}(t,u)\right) \qquad (7.11)$$

In a discretized system, the volume of the hydraulic fluid inside the accumulator at time 't' is equal to the sum of the previous state fluid volume and the product of the system flow and Δt (eq. 7.12)

$$V_{oil}(t + \Delta t) = Q_{sys}(t,u)\Delta t + V_{oil}(t) \qquad (7.12)$$

The fluid flow inside the accumulator is also equal to the rate at which the gas volume inside the accumulator is compressed. Thus, the sum of the fluid flow inside the accumulator is equal to the negative of rate of the gas volume (eq. 7.13).

$$Q_{sys}(t,u) = Q_{PM1}(t,u) - Q_{PM2}(t,u) = -\dot{V}_{gas}(t,u) \qquad (7.13)$$

The state of charge (SOC) represents the ratio of current potential energy to the full potential energy is stored in the accumulator. The SOC is derived from the discretized accumulator pressure equation (eq. 7.14) and the Ideal Gas Law equation (eq. 7.15).

$$P(t) = SOC \ (P_{max} - P_{min}) + P_{min} \tag{7.14}$$

$$V_{gas}(t) = \frac{P_{initial}V_{initial}}{P(t)} \tag{7.15}$$

The derivation of the accumulator equation starts with the discretization of the gas volume rate in the accumulator (eq. 7.16). Then, the Ideal Gas Law (eq. 7.15) and SOC definition (eq. 7.14) equations are plugged in to eq. 7.16 such that the discretized volume rate is defined in terms of pressure and SOC (eq. 7.17). Finally, eq. 7.17 is re-written as the SOC rate in terms of the gas volume rate (eq. 7.18). In the simulation, SOC is one of the control variables and this relationship relates the rate of SOC to the system flow.

$$\dot{V}_{gas} = \frac{\Delta V}{\Delta t} = \frac{V_{current} - V_{previous}}{\Delta t} \tag{7.16}$$

$$\dot{V}_{gas} = \frac{P_{initial}V_{initial}}{\Delta t} \left(\frac{P_{previous} - P_{current}}{P_{previous}P_{current}} \right) = \frac{P_{initial}V_{initial}\Delta P}{\Delta t} \left(\frac{SOC_{previous} - SOC_{current}}{P_{previous}P_{current}} \right) \tag{7.17}$$

$$\dot{SOC} = -\frac{\Delta V}{\Delta t} \frac{P_{previous}P_{current}}{P_{initial}V_{initial}\Delta P} \tag{7.18}$$

Table 7.2. Specification of accumulator

Brand/ model	Capacity (L)	Mass (kg)
Lightning hybrid composite	113.56	84.37
Lightning hybrid composite	75.17	58.06

c. Diesel engine

The engine model is used in simulation to calculate the simulation cost or fuel consumption resulting from each control decision. The engine used in this study is 10L Caterpillar 250 kW (335 HP) diesel and is represented by its fuel consumption engine map, obtained from AVL ADVISOR software (fig. 7.6). The map is based on experimental data, with

engine torque ranging from 200 Nm to 1695 Nm and the engine operational speed ranging from 68 rad/s to 219 rad/s. Although the engine speed from the map starts at 68 rad/s, the modeled engine is allowed to shut off (zero torque and speed). The engine is also allowed to operate at normal operating speed, but with very low torque (blue region in fig. 7.1 & 7.2). At such operating conditions, the fuel consumption at the same speed, but with minimal map provided torque (200 Nm), is used. At the operating condition of speed lower than idling, the torque demand has to be zero, otherwise the engine could stall. A high penalty in the simulation is applied to such operating conditions (red region in fig. 7.1 & 7.2) to ensure the engine does not stall. In the simulation, the engine motion is modeled considering its inertia (eq. 7.19).

$$T_{engine} - T_{load} = J_{engine}\dot{\omega}_{engine} \qquad\qquad (7.19)$$

Table 7.3. Specification of diesel engine

Brand	Displacement (L)	Mass (kg)	Max. torque (Nm)	Max. power (kW)
Caterpillar	10.3	932	1695 @ 125.7 rad/s	261 @ 188.5 rad/s
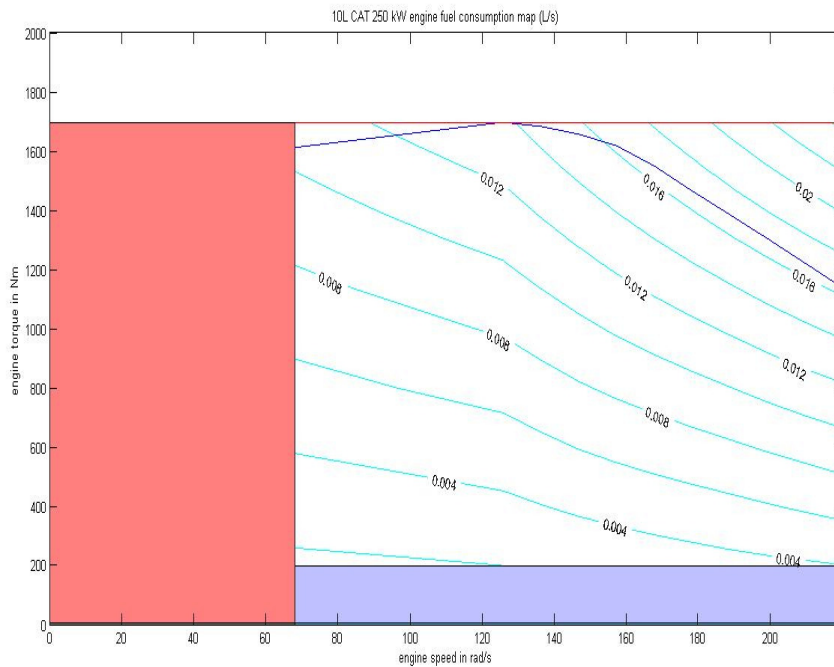
Figure 7.1. 10L caterpillar diesel engine map

10L CAT 250 kW engine efficiency map

engine torque in Nm

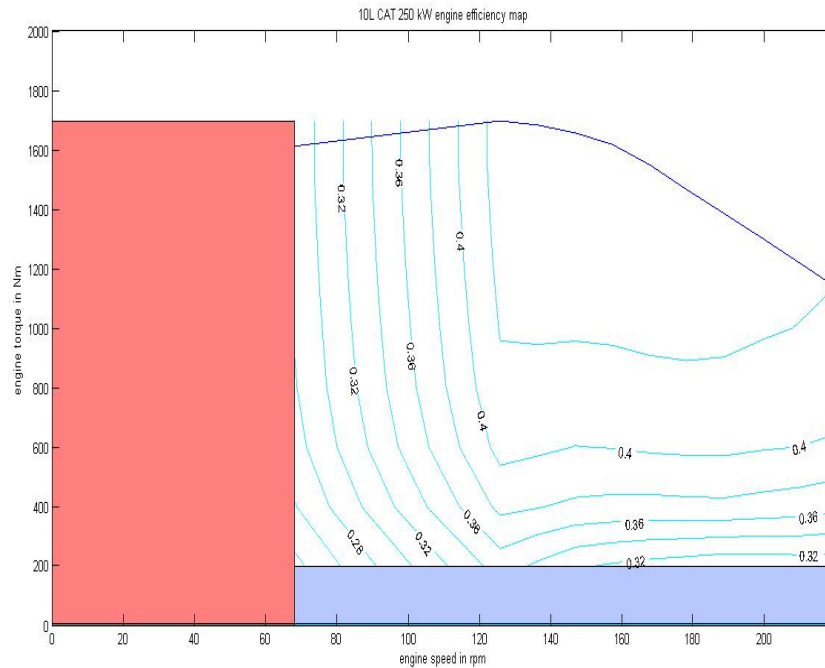engine speed in rpm

Figure 7.2. Engine map thermal efficiency

7.2 Quasi-static simulation

In quasi-static simulation, the drive cycle is discretized into multiple one-second intervals, with the assumption at each interval the average angular speed and the angular acceleration of the wheels remain constant. Each interval has current (t) and previous (t-1) states that are used to calculate the average speed and acceleration (eq. 7. 20 and 7.21)

$$\omega_{ave} = \frac{\omega_{cur}+\omega_{pre}}{2} = \frac{\omega(t)+\omega(t-1)}{2} \qquad (7.20)$$

$$\dot{\omega} = \frac{\omega_{cur}-\omega_{pre}}{\Delta t} = \frac{\omega(t)-\omega(t-1)}{\Delta t} \qquad (7.21)$$

Based on the angular speed and acceleration, the tractive torque (as discussed in chapter 3) can be calculated. The tractive torque and the wheel speed (ω_{wheel}) are the inputs for the simulation at every time interval. In a conventional drive train, these two variables should be sufficient to calculate drive train components' internal torque and angular speed. A hybrid drive train, on the other hand, utilizes more than one energy source to propel and requires a good

supervisory controller that can manage the power optimally for all HMT configuration candidates described in Chapter 5.

7.2.1 Deterministic Dynamic Programming (DDP)

DDP technique is used as the optimal supervisory controller to minimize fuel consumption and to ensure the simulation ends at the same SOC as the initial (eq. 7.25).

$$\min(fuel\ consumed) = \min\ (\int_{t_i}^{t_f} \dot{m}_f(t,u)\ dt),$$

Boundary condition: $SOC_i = SOC_f$ (7.25)

The DDP numerical simulation needs discretization of cost function and the physical constraints are implemented through penalties (eq. 7.26). The penalties increase the costs to near infinity whenever the control decision causes one of the components to operate beyond its limit.

$$\min(Cost(J)) = min\ \left(\sum_{k=1}^{N} \dot{m}_f(t,u) + \text{penalties}\right)$$

Boundary condition: $SOC_{k=1} = SOC_{k=N}$ (7.26)

DDP algorithm runs backwards, from the terminal stage ($k = N$) to the initial stage, ($k = 1$). The algorithm calculates the minimum cost to reach the terminal stage from the previous stage (N-k) (left side of eq. 7.27). The algorithm starts with the calculation of transition cost from one combination of controls at the previous stage (red box in fig. 7.3) to all combinations of control decisions at current stage (green middle box in fig. 7.3).

$$J_{N-k}{}^*(X(N-k)) = min_{U(N-k)}\ \{(transition\ cost) + J_{N-k+1}{}^*\ (f(X(N-k), U(N-k))\}$$
(7.27)

The arrows in fig. 7.3 represents the transition cost calculations. The transition costs are then added to the minimum cost to reach the terminal stage from the current stage. The sums are saved as cost candidates of the previous state.
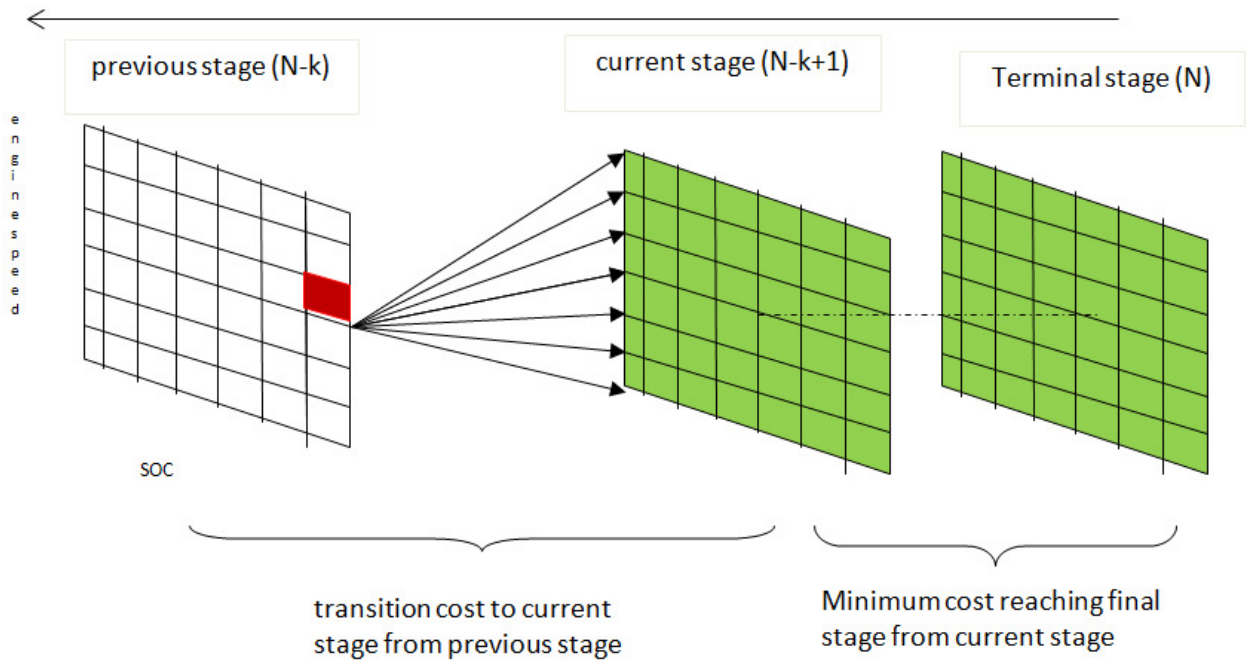
Figure 7.3. DDP data management structure

The minimum value among the cost candidates is now saved as the minimum cost to reach the terminal stage from the one combination of controls at that previous stage (red box in fig. 7.3). The same process is repeated for other control combinations from the previous stage. Once the cost matrix for previous stage is filled with the minimum cost to reach the terminal stage, the algorithm moves one step backward (k-1) and starts the same cycle all over again until it reach the initial stage k=1.

7.3 Matlab adaptation

Matlab functions are used to implement the DDP optimal simulation for the HMT hybrid configuration candidates running on the three drive cycles. The implementation of the Matlab code can be divided into three function stages; pre-process, simulation, and post-process.

a. Stage 1: Pre-process function

This stage prepares the simulation before it begins. It defines vehicle component specifications, drive cycle, time step size, simulation time frame, control variables step sizes, and initial conditions (initial and final SOC).

b. Stage 2: Simulation function

The simulation function starts from the final time of the time frame, T_{final}, and ends at the beginning of the simulation time frame, $T_{initial}$. At the final time stage, the terminal condition is applied by assigning high costs to undesirable final states in the terminal cost matrix. For example, when the terminal cost matrix is assigned with zero cost at the SOC = 0.5 and 1e6 cost at other states, this would force the simulation to converge into the desirable SOC value (SOC = 0.5). At each time step, the cycle described in 7.2.2 is used and by the time the simulation is finished, the cost matrix becomes very large.

c. Stage 3: Post-processing function

The post-processing function is performed only when the simulation function (stage 2) is done. At this stage, the cost matrix is filled with a plethora amount of data and not all of the data are useful. The post-processing function selects only the meaningful data to be plotted and calculated. The minimum number in the initial cost matrix is the minimum fuel consumed by the drive train to complete the drive cycle. This minimum fuel consumption is used to calculate the fuel economy in MPG of the simulation. The control optimal solution is obtained by running the cost matrix forward, from the initial to the final time frame.

This chapter shows the drive train components models used in the optimal simulation and how to implement the DDP simulation in Matlab. The simulations were done for the HMT configuration candidates and the results are shown in the next chapter.

Chapter 8

Simulation results and discussion

HMT configuration candidates from chapter 6 are modeled and simulated via DDP on Manhattan, NYC, and CBD city bus drive cycles. For the single-staged HMT, the configuration is classified by coupling type (output- or input- coupled) and S_{crit} value. The dual-staged HMT is classified by S_{crit} value alone. The optimal configuration is the configuration that allows both the engine and transmission (HMT hybrid) to work most efficiently at city bus driving conditions, and should reflect on the fuel economy simulation results. The configurations that fail in the simulation are the ones that cause a drive train component to operate beyond its physical limitations.

8.1 Single staged HMT: Input-coupled HMT

Table 8.1. Fuel economy results for six input-coupled HMT configurations

S_{crit}	Configuration	Manhattan (MPG)	NYC (MPG)	CBD (MPG)
0.28	IRC, $h = \frac{72}{28}$	failed	failed	3.945
0.30	IRC, $h = \frac{7}{3}$	failed	failed	3.937
0.40	IRC, $h = \frac{3}{2}$	4.537	failed	7.323
0.45	IRC, $h = \frac{55}{45}$	4.350	failed	7.545
0.48	IRC, $h = \frac{52}{48}$	4.227	3.042	7.370
0.52	ISC, $h = \frac{52}{48}$	4.349	4.096	7.656

The fuel economy simulation results for input-coupled HMT configuration candidates are shown in table 8.1. The input coupled HMT configuration with S_{crit} value of 0.52 achieves the highest fuel economy among the input-coupled HMT HHB configurations, with the average fuel economy of 5.37 MPG. The configuration performs at its best on the CBD drive cycle with 7.66 MPG fuel economy. The inout coupled HMT configurations with S_{crit} value of 0.28, 0.3, 0.4 and 0.45 fail to satisfy the torque and the speed demands of at least one of the city bus drive cycles.
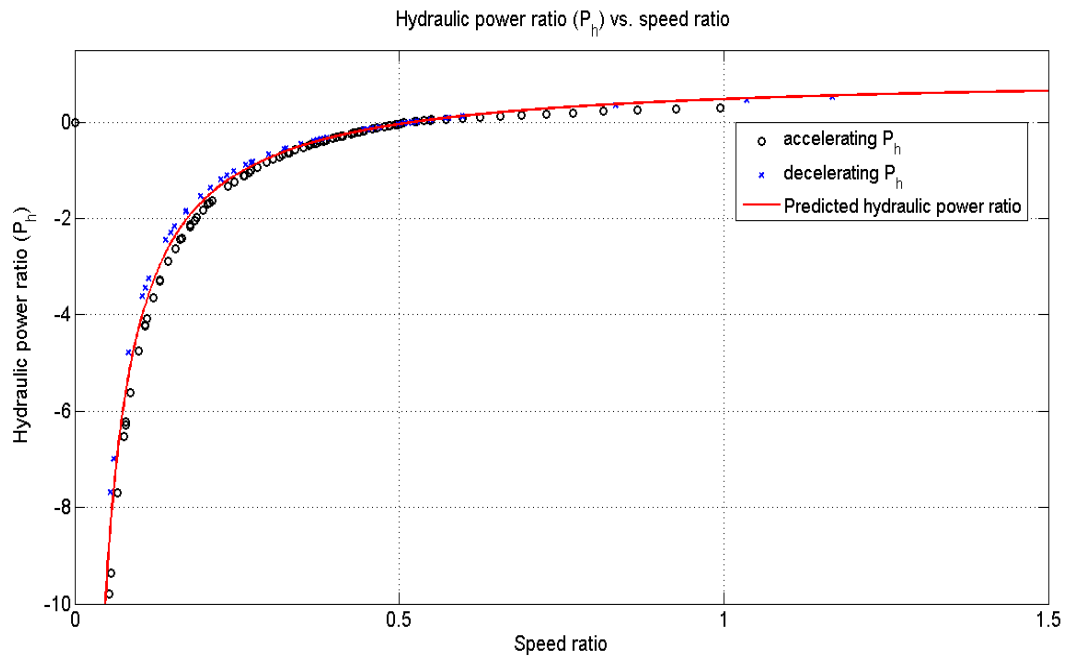
Figure 8.1. P_h vs. ω_{rat} plot for the input-coupled HMT withS_{crit} =0.52 on CBD drive cycle

The $\boldsymbol{P_h}\ \boldsymbol{vs.}\ \boldsymbol{\omega_{rat}}$ plot for the input-coupled HMT with $\boldsymbol{S_{crit}}$ of 0.52 simulated on the CBD drive cycle, is shown in fig. 8.1. The plot shows the $\boldsymbol{P_h}$ values when the vehicle is accelerating or at constant speed (the black 'o' points) and decelerating (the blue 'x' points). The plot shows $\boldsymbol{P_h}$ values from both the accelerating and decelerating events follow the predicted $\boldsymbol{P_h}$ line (the red line) closely along the speed ratio range. The drive train uses the hydraulic power re-circulation

(HPR) mode at speed ratios lower than the critical ($S_{crit} = 0.52$) and uses normal HMT mode as speed ratios higher than the critical, as predicted in the kinematic study (fig. 8.2).
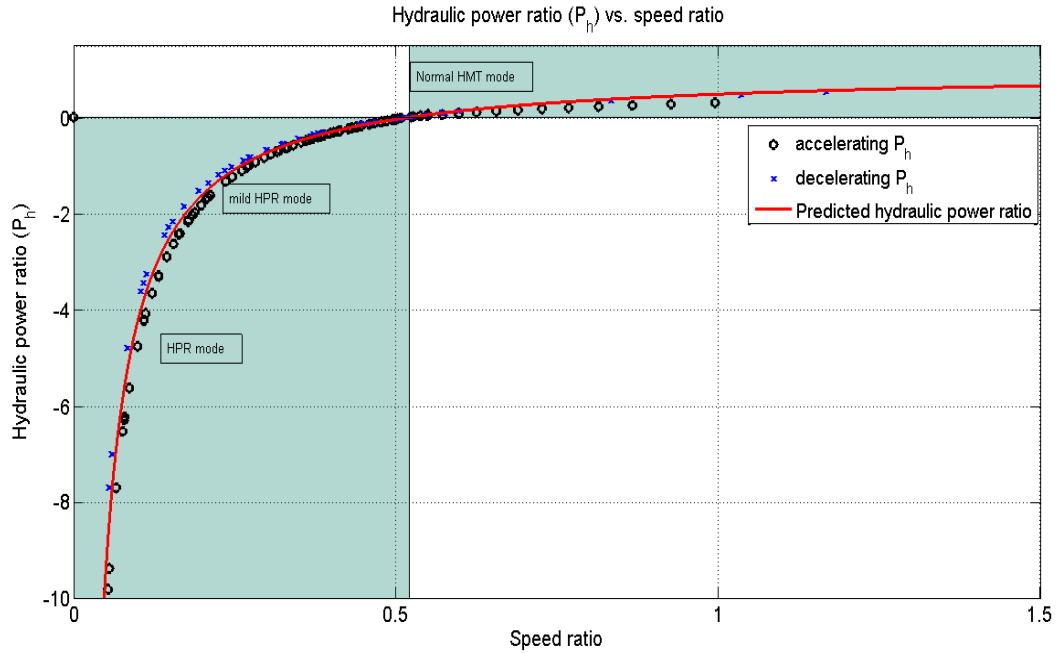

Figure 8.2. input-coupled HMT with S_crit =0.52 on CBD drive cycle HMT operating modes

The DDP decides to operate mostly in the mild HPR (P_h values close to zero) and the normal power-split modes (fig 8.2). The HPR mode usage frequency decreases as $P_h < -2$ due to the transmission efficiency being low at that range (table 5.3). The simulation results also show that some of the P_h values do not exactly follow the predicted ones (red line). The discrepancies are due to the hydraulic accumulator activity releasing and absorbing its energy.

The optimized control strategy for input-coupled HMT shows that the modes used are strictly limited to the normal power-split and the HPR (fig. 8.3). The mode pattern is predictable, as the HPR mode is used when the wheel torque required is high, such as when accelerating at low speed and the normal mode is used when the torque demand is low.
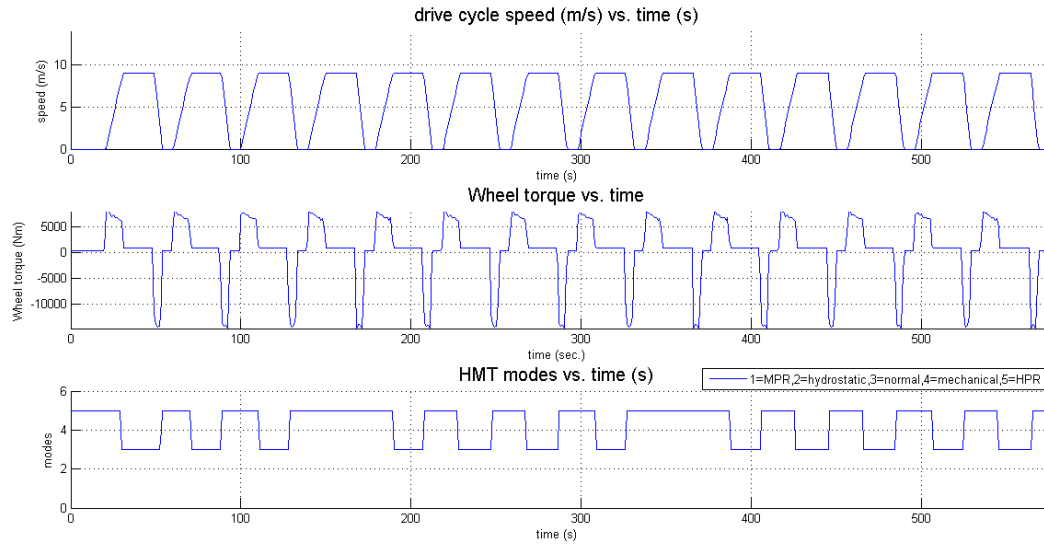
8.2 Output-coupled HMT

Table 8.2 Fuel economy results for six output-coupled HMT configurations

S_{crit}	Configuration	Manhattan (MPG)	NYC (MPG)	CBD (MPG)
0.52	RSO, $h = \frac{52}{48}$	3.910	2.019	7.678
0.6	RSO, $h = \frac{3}{2}$	4.513	3.043	8.266
0.62	RSO, $h = \frac{62}{38}$	4.757	3.068	8.482
0.65	RSO, $h = \frac{65}{35}$	5.078	3.095	8.622
0.68	RSO, $h = \frac{68}{32}$	5.393	3.383	failed
0.7	RSO, $h = \frac{7}{3}$	failed	3.576	failed

The fuel economy simulation results for output-coupled HMT configuration candidates are shown in table 8.2. The output coupled HMT configuration with S_{crit} value of 0.65 performs

64

the best among the single-staged HMT, with the average fuel economy of 5.59 MPG. Like the input-coupled HMT, this configuration performs its best on the CBD drive cycle, achieving 8.62 MPG. The configurations with S_{crit} value of 0.68 and 0.7 failed to provide the torque and the speed required by CBD and Manhattan drive cycles.
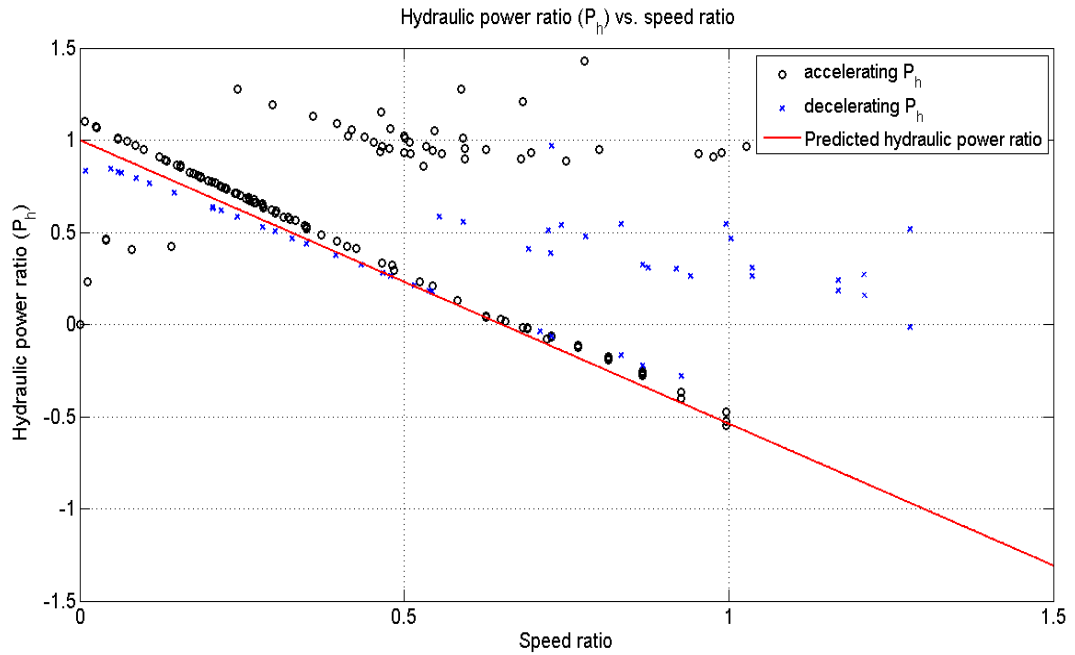

Figure 8.4. P_h vs. ω_{rat} plot for the output-coupled HMT with S_{crit} =0.65 on CBD drive cycle

The P_h $vs.$ ω_{rat} plot from simulation (fig. 8.4) shows the P_h values when the vehicle is accelerating (also at constant speed) and decelerating. Both of them follow the linear P_h pattern, as predicted in the kinematic study. There is also a group of simulated P_h values that do not follow the predicted line. This group tends to be around P_h value of 1.0 (hydrostatic mode) when accelerating and P_h value of 0.5 (normal HMT mode) when decelerating. Despite the discrepancies due to the HPA activities, the majority of P_h points still follow the same pattern as predicted in the kinematic study.
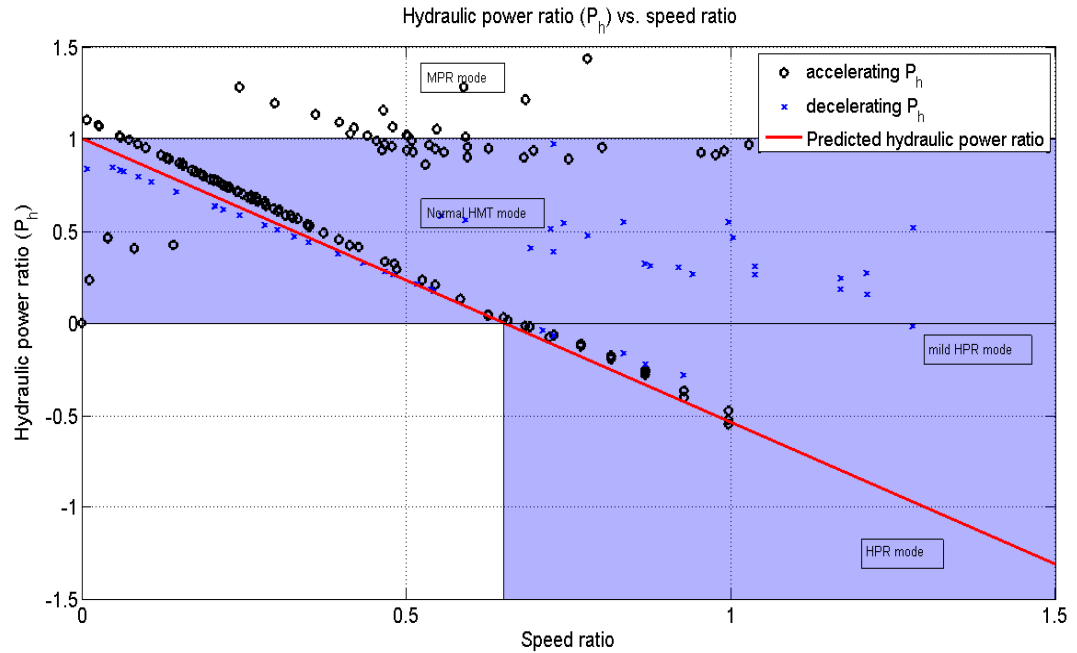
Figure 8.5 output-coupled HMT with S_{crit}=0.65 on CBD drive cycle HMT operating modes

The optimized control strategy for output-coupled HMT shows that the mode pattern is not as predictable as in the case of the input-coupled HMT (fig. 8.6). Unlike the input-coupled HMT, the output-coupled drive train mostly uses the normal power-split mode during the high torque and low speed demand (fig. 8.6). It can also be seen that the use HPR mode is kept minimal and most of the HPR mode usage is in the high-efficiency mild region (fig 8.5). There are also occasions where the low-efficiency MPR mode is used, but they usually only last one second each time. They are also used when the torque demand decreases after the peak torque is reached. This might be the control strategy's way of emptying the accumulator before it can be charged again for the next acceleration cycle.

8.3 Dual-staged HMT

Chapter 6 shows the dual-staged HMT combines an input- and an output-coupled configuration, with the same S_{crit} values, in one transmission.
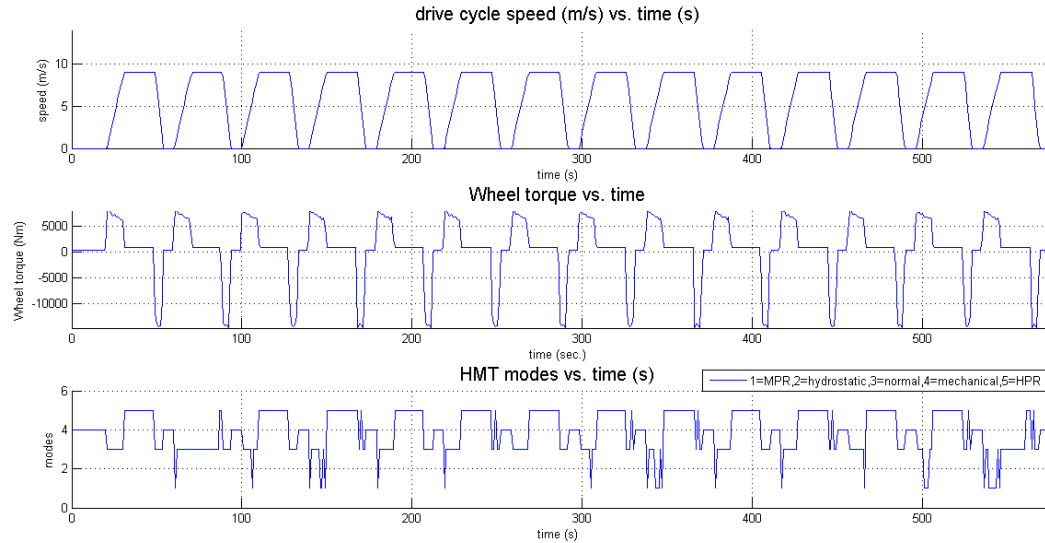
66

Figure 8.6. Speed, wheel torque and HMT modes for the output-coupled HMT with S_{crit}= 0.65 on CBD

This requires two PGS units (PGS1 and PGS2). PGS1 is located at the input shaft and is connected the same way as an output-coupled HMT's. PGS2 is located at the output shaft and is connected the same way as an input-coupled HMT's (table 8.3).

Table 8.3. Fuel economy results for five dual-staged HMT configurations

S_{crit}	PGS 1 conf.	PGS 2 conf.	Manhattan (MPG)	NYC (MPG)	CBD (MPG)
0.4	SRO, $h = \frac{3}{2}$	IRC, $h = \frac{3}{2}$	4.164	3.390	6.722
0.45	SRO, $h = \frac{55}{45}$	IRC, $h = \frac{55}{45}$	4.218	3.563	6.817
0.48	SRO, $h = \frac{52}{48}$	IRC, $h = \frac{52}{48}$	4.156	3.576	6.946
0.52	RSO, $h = \frac{52}{48}$	ISC, $h = \frac{52}{48}$	4.088	3.921	7.269
0.60	RSO, $h = \frac{3}{2}$	ISC, $h = \frac{3}{2}$	3.958	4.559	9.311

The dual-staged HMT are designed such that it operates as output-coupled HMT when the speed ratio is less than the critical value (S_{crit}) and as input-coupled HMT when the speed ratio is greater than the critical value (S_{crit}) (fig. 6.3). The DDP simulation results (table 8.3)

67

show similar fuel economy among different configurations in the dual-staged HMT architecture. The dual-staged HMT with $S_{crit} = 0.6$ achieves the highest fuel economy for CBD drive cycle (9.31 MPG), an 8% increase in fuel economy compared to the optimized single-staged HMT.
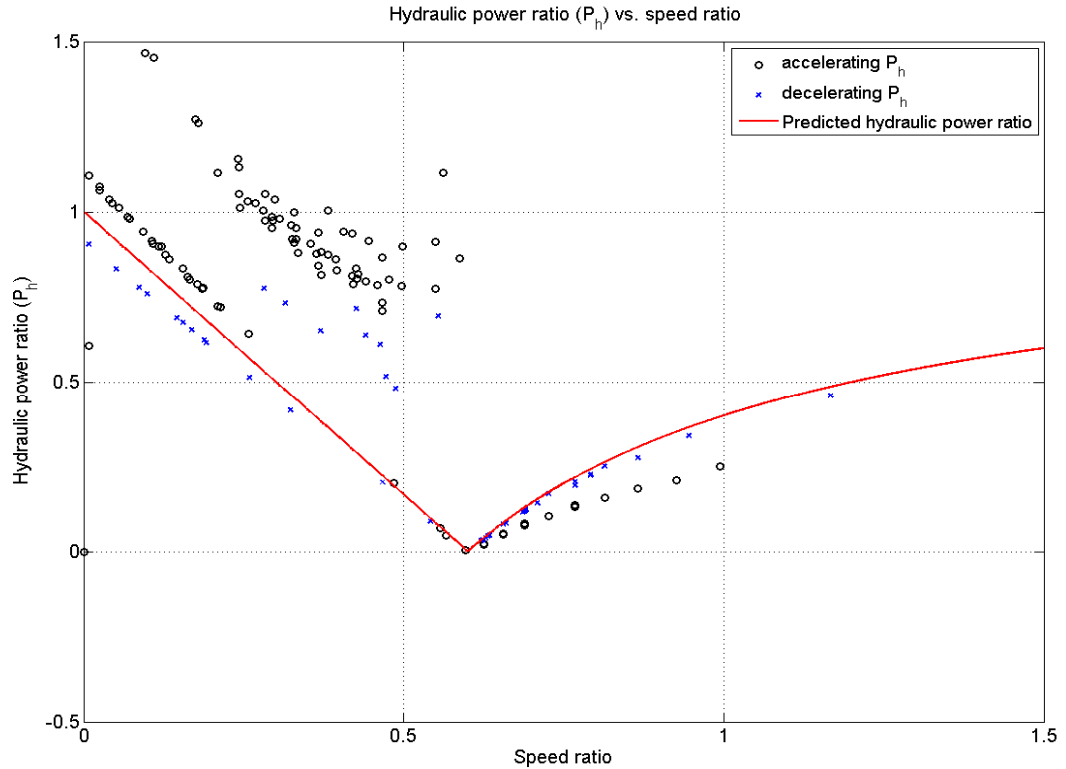

Figure 8.7. P_h $vs.$ ω_{rat} plot for the dual-staged HMT with S_{crit} = 0.6 on CBD

The DDP control decision for dual-staged HMT (fig. 8.7) shows it behaves like an output-coupled HMT until it reaches the critical speed ratio, after which it behaves like an input-coupled HMT to avoid the operation in HPR mode $(P_h < 0)$, as predicted. The dual-staged HMT drive train mostly operates in normal HMT mode and occasional use of the HPR can be seen due to the hydraulic accumulator activities, absorbing and releasing the hydraulic power (fig. 8.9). The simulation also shows the dual-staged HMT operates mostly as an output-coupled HMT (at low speed ratio). Thus the occasional use of the MPR mode to deplete the accumulator charge

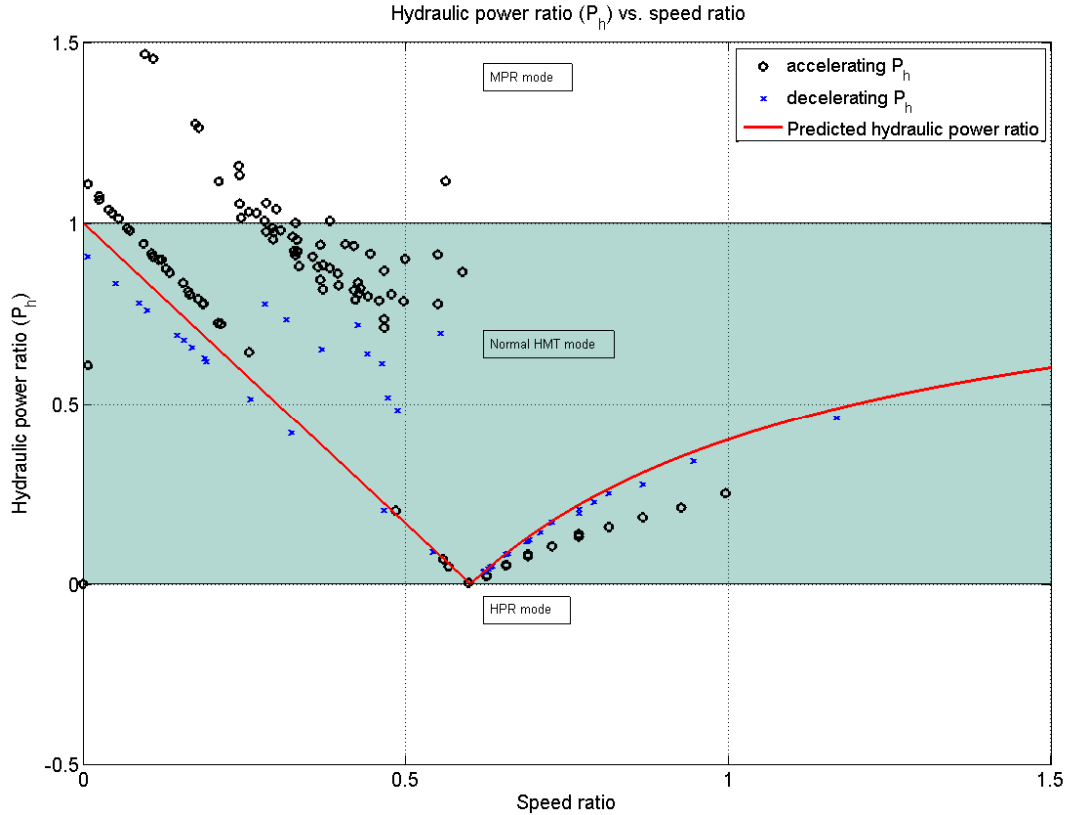in preparation for the next acceleration cycle, as in the case of output-coupled HMT, can be seen.

Figure 8.8. Dual-staged HMT with S_{crit}=0.60 on CBD drive cycle HMT operating modes

8.4 Simulation results discussion

This chapter puts HMT parameter and operating mode studies to test by simulating the HMT configuration candidates. Overall, the HMT hybrid drive train behaves like a transmission, judging by how the simulated P_h values follow the predicted values in the kinematic study, which does not include energy storage capability. The HMT mode study is also proven correct as the optimal control strategy keeps the drive train mode within the normal HMT and mild HPR modes. There are very few occasions where the low-efficiency MPR mode is used in output-coupled and dual-staged HMTs. It is used very briefly (one second each time), usually right

before the drive cycle decelerates. This might be the optimal control strategy's way of emptying

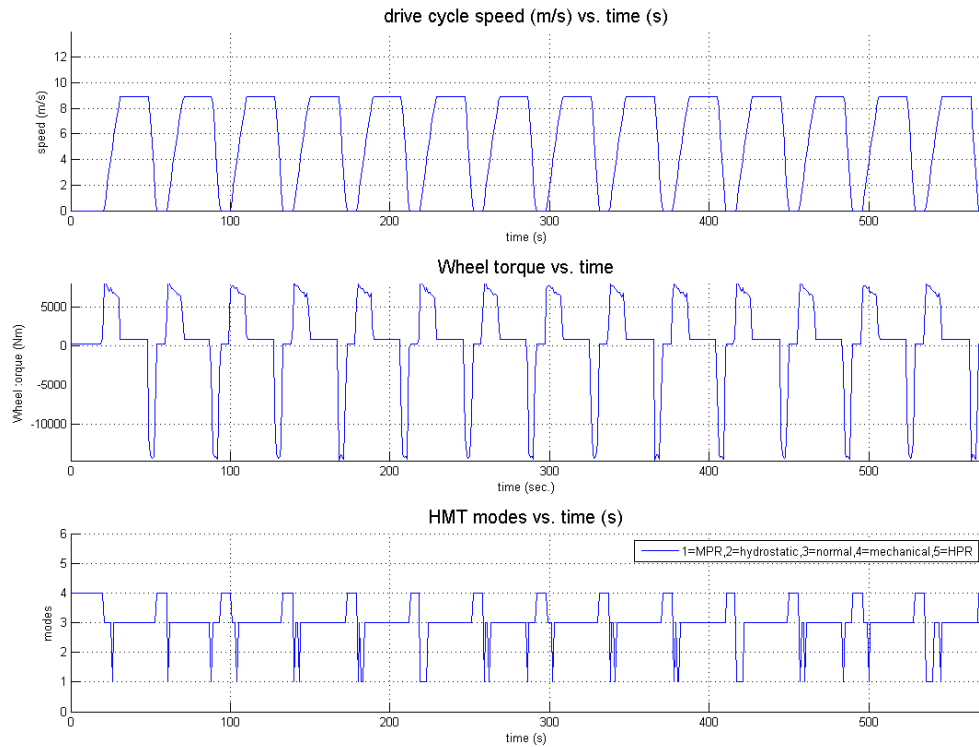the accumulator before it can be charged again during the deceleration.

Figure 8.9. Speed, wheel torque and HMT modes for the dual-staged HMT with S_{crit}= 0.6 on CBD

The simulation reveals that the dual-staged HMT offers the best fuel economy among

the three types. However, the single-staged HMT best fuel economy is not much worse (dual

staged-HMT improves the fuel economy only by 8%). The dual-staged HMT is more complex to

implement than the single-staged because it involves two PGS's, and involves shifting between

input-and output-coupled modes, which could cause performance discontinuity and require

extensive automatic clutches control to ensure smooth operation. Thus, the output-coupled

HMT with S_{crit} value of 0.65 is chosen to be the suitable configuration for the HMT hydraulic

hybrid city bus.

Chapter 9

Conclusion

9.1 Review

This research finds the optimal power-split drive train for hybrid hydraulic city bus by studying power-split architecture configurations. Sung shows that there are 12 single-staged HMT configurations and each of them has its own characteristics [37]. Cheong shows the configurations are not unique, where each configuration can become another with the manipulations of planetary gear ratio 'h' [6]. The essences of these two power-split architecture studies are utilized in this research. This research classifies power-split configurations using the critical speed ratio. This way, the idea of a specific configuration having unique characteristics, and that configurations can be realized with the manipulations of planetary gear ratio 'h', still holds. This classification system greatly simplifies the search for the optimal configuration, and can also be used in dual-staged HMT. The critical speed ratio classification method can be converted back into the twelve configurations with its planetary gear ratio by using the generalized hydraulic power ratio equations (eqs 6.1 & 6.2), so that the physical drive train can be built.

The optimal simulation candidates are chosen among output-coupled, input-coupled and dual-staged HMTs. The dual-staged HMT with S_{crit} value of 0.60 achieves the best fuel

economy among all candidates and the output-coupled HMT with S_{crit} value of 0.65 achieves second-best. The more complex dual-staged HMT drive train gained only 8% more fuel economy than the single-staged output-coupled. This research chooses the output-coupled candidate as its optimal drive train for city bus because not only can it get good fuel economy, it is also much simpler to build, control, and maintain than the dual-staged HMT candidate. The output-coupled HMT S_{crit} value of 0.65 is converted back into the physical configuration of the RSO with the planetary gear ratio of 65/35 (table 9.1).

Table 9.1. Specification of optimal HMT HHB

Engine	Caterpillar C-10, 10L 250kW Diesel	Hydraulic pump/motor 1	A4VG250 250 cc/rev
Input shaft speed reducer gear ratio	0.937	Hydraulic pump/motor 2	A4VG250 250 cc/rev
Output shaft speed reducer gear ratio	6.202	Accumulator size	113.56 L
PGS location	Input shaft	Max pressure	41.4 MPa
Configuration	RSO	Vehicle mass (with 40 passengers)	14783 kg
Planetary gear ratio (R/S)	65/35	Vehicle curb mass	12945 kg

9.2 contributions

The primary accomplishment of this research can be boiled down to the discovery of a unique critical speed ratio(S_{crit}) in any specific HMT configuration. The representation of HMT configuration using the critical speed ratio greatly simplifies the optimization of HMT configuration because instead of studying every possible configuration, the HMT drive train optimization problem is reduced to finding for the suitable S_{crit} value for the specified

application. The S_{crit} value and the generalized forms are used to find the configuration's planetary gear ratio and how they are connected, so that a physical drive train can be built.

This research also establishes that there are two kinds of power re-circulation modes, HPR and MPR. In many studies, any power re-circulation is viewed as inefficient and many turned to using the more complex dual-staged HMT architecture to avoid such mode. This study shows the hydraulic power re-circulation (HPR) mode has a usable range with better efficiency than the hydrostatic mode and is often used by the optimal control strategy. Another power re-circulation mode is the mechanical power re-circulation (MPR), which is inefficient and is eliminated by design. This discovery of good range of power re-circulation mode proves the more complex dual-staged HMT is not necessarily the optimal architecture in heavy duty drive train.

9.3 recommendations for future work

The quasi-static simulation ignores the transient aspect of the engine and the fuel economy results could differ from the simulation. The proposal for this research included a plan to use the hydrostatic dynamometer to compare the simulation and the experimental results. However, there is no reliable method of representing the 250kW bus engine using the small 86 kW (the diesel engine currently mounted to the dynamometer). In the future, a bigger diesel engine should be mounted to the dynamometer so that more heavy-duty applications, such as this HHB, can be tested.

In this research, the HMT HHB is modeled on Orion VII HEB bus and the pump/motor efficiency maps are derived from a generic swash plate pump/ motor. The existence of a lightweight Altair series HHB shows with the specially designed chassis and the use of high-

efficiency hydraulic pump/ motor, the HHB can achieve high fuel economy. In the case of this

HMT HHB, there is still room for improvement through better component and chassis design.

References

1. Barnitt, R., "In-Use Performance Comparison of Hybrid Electric, CNG, and Diesel Buses at New York City Transit," SAE Technical Paper 2008-01-1556, 2008, doi:10.4271/2008-01-1556.

2. Baseley, S., Ehret, C., Greif, E., and Kliffken, M., "Hydraulic Hybrid Systems for Commercial Vehicles," SAE Technical Paper 2007-01-4150, 2007, doi:10.4271/2007-01-4150.

4. Burke, A., "Saving Petroleum with Cost-Effective Hybrids," SAE Technical Paper 2003-01-3279, 2003, doi:10.4271/2003-01-3279.

5. Carl, B., Ivantysynova, M., and Williams, K., "Comparison of Operational Characteristics in Power Split Continuously Variable Transmissions," SAE Technical Paper 2006-01-3468, 2006, doi:10.4271/2006-01-3468.

6. Cheong K. "Optimal design of power-split transmissions for hydraulic hybrid passenger vehicles," Proceedings of the American Control Conference 2011:3295-300.

7. Chiang, P., "Two-Mode Urban Transit Hybrid Bus In-Use Fuel Economy Results from 20 Million Fleet Miles," SAE Technical Paper 2007-01-0272, 2007, doi:10.4271/2007-01-0272.

8. Clark, N.N., Zhen, F., Wayne, W. S., and Lyons, D.W. "Transit Bus Life Cycle Cost and Year 2007 Emissions Estimation," U.S. Department Of Transportation Federal Transit Administration (FTA), July 2, 2007, FTA-WV-26-7004.2007.1

9. Dickens, M., Neff, J. (2012). "2012 public transportation fact book 63rd edition," American public transportation association (APTA). < http://www.apta.com>

10. Finley, B. and Daly, T., "A Three Year Comparison of Natural Gas and Diesel Transit Buses," SAE Technical Paper 1999-01-3738, 1999, doi:10.4271/1999-01-3738.

11. Fussner, D. and Singh, Y., "Development of Dual Stage Input Coupled Split Power Transmission Arrangements and their Characteristics," SAE Technical Paper 2002-01-0590, 2002, doi:10.4271/2002-01-0590.

12. Fussner, D., Wendel, G., and Wray, C., "Analysis of a Hybrid Multi-Mode Hydromechanical Transmission," SAE Technical Paper 2007-01-1455, 2007, doi:10.4271/2007-01-1455.

13. Guo Qing L. "Optimal design for a hydraulic regeneration propel system of the hydraulic hybrid bus." WSEAS Transactions on Systems 2010;9(5):453-62.

14. Guzzella LS, Antonio., "Vehicle propulsion systems: Introduction to modeling and optimization," Springer 2007.

15. Han, Z., Yuan, Z., Guangyu, T., Quanshi, C. et al., "Optimal Energy Management Strategy for Hybrid Electric Vehicles," SAE Technical Paper 2004-01-0576, 2004, doi:10.4271/2004-01-0576.

16. Hayashi, T., Saito, M., Yoshida, Y., and Nanri, T., "Advanced Hydro-Mechanical Transmission with High-Durability for Small Utility Vehicles," SAE Technical Paper 2001-01-0876, 2001, doi:10.4271/2001-01-0876.

17. Heskitt, M. (2012), "Design & Development of the LCO-140H Series Hydraulic Hybrid Low Floor
    Transit Bus," Federal Transit Administration No. 0018

18. Hewko, L.O.; Weber, T.R., "Hydraulic Energy Storage Based Hybrid Propulsion System For A Terrestrial
    Vehicle," Energy Conversion Engineering Conference, 1990. IECEC-90. Proceedings of the 25th
    Intersociety, vol.4, no., pp.99,105, 12-17 Aug 1990 doi: 10.1109/IECEC.1990.716464

19. Kargul J. J., "Affordable hybrids for a petroleum and carbon constrained world," 2012 NTEA Work
Truck Show,
     March 6, 2012

20. Karnopp D, Margolis DL, Rosenberg RC. "System dynamics: Modeling and simulation of mechatronic
    systems," John Wiley & Sons; 2006. .

21. Kumar, R. " Investigation of Various Power Management Strategies for a Class of Hydraulic Hybrid
Powertrains:
    Theory and Experiments," Proceedings of 6th Fluid Power Net International

22. Kellaway, M.J., "Hybrid buses—What their batteries really need to do," Journal of Power Sources,
    Volume 168, Issue 1, 25 May 2007, Pages 95-98, ISSN 0378-7753,

23. K. Masuzawa, K. Ichiryu., "Basic study on input split type hydro-mechanical transmission", Proceedings
    of the International Conference on Fluid Power; 2001.

24. Li,C.T., Peng, H. "Optimal configuration design for hydraulic split hybrid vehicles," American Control
    Conference(ACC), 2010 , vol., no., pp.5812,5817, June 30 2010-July 2 2010

25. Li, P., Mensing, F. (2010). Optimization and Control of a Hydro-Mechanical Transmission based Hybrid
Hydraulic
    Passenger Vehicle. 7th International Fluid Power Conference

26. Derong L.; Ning J., "Finite horizon discrete-time approximate dynamic programming," Computer Aided
    Control System Design, 2006 IEEE International Conference on Control Applications, 2006 IEEE
    International Symposium on Intelligent Control, 2006 IEEE , vol., no., pp.446,451, 4-6 Oct. 2006

27. Liu, G.Q.; Yan, Y, "Simulation and experimental validation study on the drive performance of a new
    hydraulic power assist system," Intelligent Vehicles Symposium, 2009 IEEE , vol., no., pp.966,970, 3-5
    June 2009

28. Liu, X; Wang, W;, "Research for energy management mode of parallel hydraulic hybrid
    vehicle," Electronic and Mechanical Engineering and Information Technology (EMEIT), 2011
    International Conference on , vol.7, no., pp.3824,3827, 12-14 Aug. 2011

29. Macor, A. (2011)., "Optimization of hydro-mechanical power split transmissions," Mechanism and
    Machine Theory, 46(12), 1901-1919. doi:10.1016/j.mechmachtheory.2011.07.007

30. Matheson, P. and Stecki, J., "Development and Simulation of a Hydraulic-Hybrid Powertrain for use in
    Commercial Heavy Vehicles," SAE Technical Paper 2003-01-3370, 2003, doi:10.4271/2003-01-3370.

31. Meisel, J., "An Analytic Foundation for the Toyota Prius THS-II Powertrain with a Comparison to a Strong Parallel Hybrid-Electric Powertrain," SAE Technical Paper 2006-01-0666, 2006, doi:10.4271/2006-01-0666.

32. Merritt H.E. Hydraulic control systems. John Wiley & Sons; 1967 .

33. Petric, J., "A Power-Split Hybrid Hydraulic Vehicle Transmission Modeling and Comparative Analysis," SAE Technical Paper 2010-01-2010, 2010, doi:10.4271/2010-01-2010.

34. Pourmovahed AA, Beachley NH, "Modeling of a Hydraulic Energy Regeneration System: Part II—Experimental Program," J. Dyn. Sys., Meas., Control. 1992;114(1):160-165. doi:10.1115/1.2896498.

35. Rossetti,A., Macor,A., "Multi-objective optimization of hydro-mechanical power split transmissions, Mechanism and Machine Theory," Volume 62, April 2013, Pages 112-128, ISSN 0094-114X,

36. Sciarretta, A., Dabadie, J., and Albrecht, A., "Control-Oriented Modeling of Power Split Devices in Combined Hybrid-Electric Vehicles," SAE Technical Paper 2008-01-1313, 2008, doi:10.4271/2008-01-1313.

37. Sung D, Hwang S, Kim H., "Design of hydromechanical transmission using network analysis," Proceedings of Institution of Mechanical Engineers Partt D: Journal of Automobile Engineering 2005;219(1):53-63.

38. Surampudi, B., Nedungadi, A., et al., "Design and Control Considerations for a Series Heavy Duty Hybrid Hydraulic Vehicle," SAE Technical Paper 2009-01-2717, 2009, doi:10.4271/2009-01-2717.

39. Triet, H., & Ahn, K. (2011)., "Comparison and assessment of a hydraulic energy-saving system for hydrostatic drives," Proceedings of the Institution of Mechanical Engineers, Part I: Journal of Systems and Control Engineering, 225(1), 21-34.

40. United States Environmental Protection Agency. "Regulatory Announcement. Heavy-duty engine and vehicle standards and highway diesel fuel sulfur control requirements," <http://www.epa.gov/otaq/diesel.htm>

41. Van B., "Hydraulic Hybrid Vehicle Energy Management System," SAE Technical Paper 2009-01-1772, 2009, doi:10.4271/2009-01-1772.

42. Van de Ven, J. D., Olson, M. W., & Li, P. Y. (2008)., "Development of a hydro-mechanical hydraulic hybrid drive train with independent wheel torque control for an urban passenger vehicle," Proceedings of the national conference on fluid power; 2008. .

43. Wang B, Luo Y, "Simulation of city bus performance based on actual urban driving cycle in china," International Journal of Automotive Technology 2008;9(4):501-7.

44. Wayne WS, Clark NN, "A comparison of emissions and fuel economy from hybrid-electric and conventional-drive transit buses." Energy Fuels 2004;18(1):257-70.

45. Walkowicz, K DOE/NREL "New York City Transit Diesel Hybrid- Electric buses: Final Results," http://www.afdc.doe.gov July 2002

46. Walkowicz, K DOE/NREL "King County Metro Transit Hybrid Articulated Buses: Final Evaluation Results,"
    Technical Report NREL/TP-540-40585 December 2006

47. Wu B, Lin CC, Filipi Z, "Optimal power management for a hydraulic hybrid delivery truck," Vehicle
    System Dynamics 2004;42(1-2):23-40.

48. Ye Cui Y. "Parameter design strategies of a parallel hydraulic hybrid bus," 2008 IEEE Vehicle Power and
    Propulsion Conference, VPPC 2008 2008.

49. Yoshida Y., "New generation hydraulic-mechanical transmission with lock-up mechanisms and
    automatic start clutch," SAE International Journal of Engines 2009;1(1):1381-8.

50. Cessna fluid power division "Cessna model 76100 hydrostatic drive" Specification sheet No. 76100

Appendices

Appendix a. PM efficiency maps in motor mode.
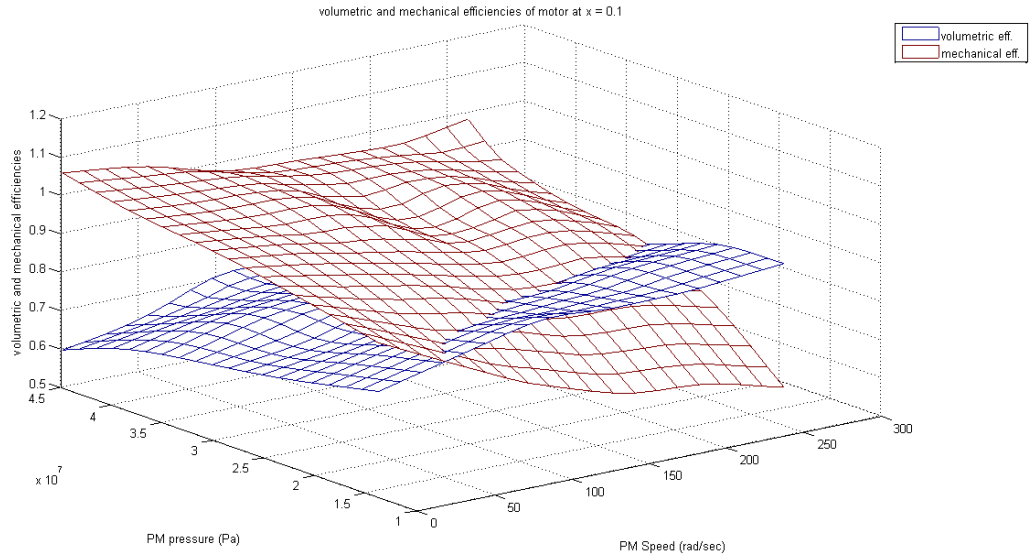
Figure a.1. PM mechanical and volumetric efficiencies in motor mode at x = 0.1
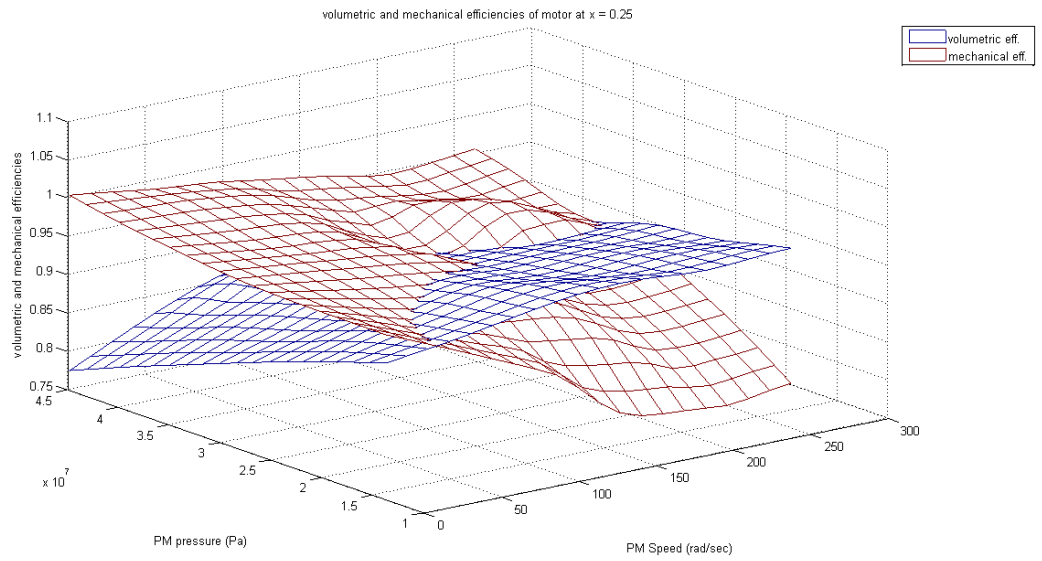
Figure a.2. PM mechanical and volumetric efficiencies in motor mode at x = 0.25
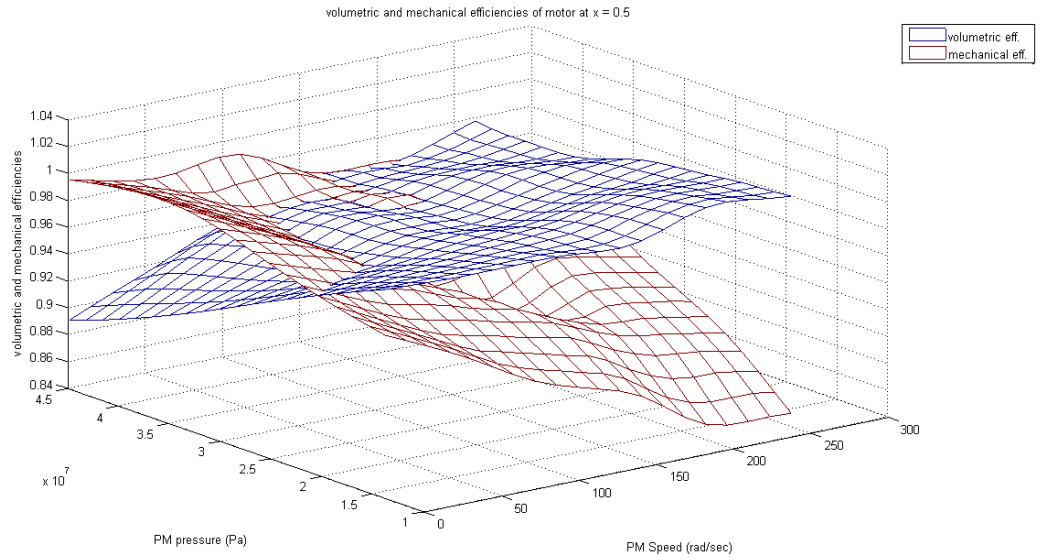
Figure a.3. PM mechanical and volumetric efficiencies in motor mode at x = 0.5
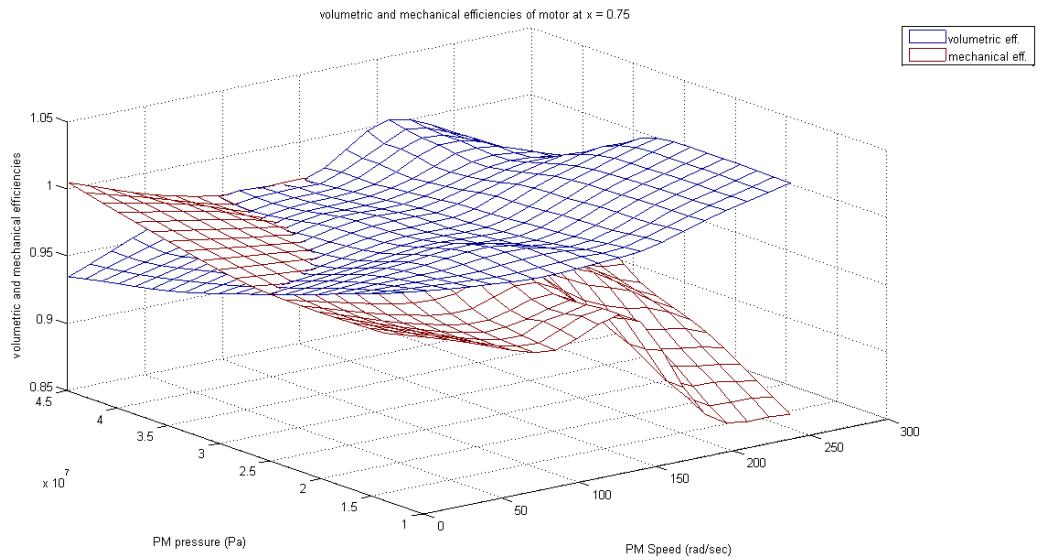
Figure a.4. PM mechanical and volumetric efficiencies in motor mode at x = 0.75
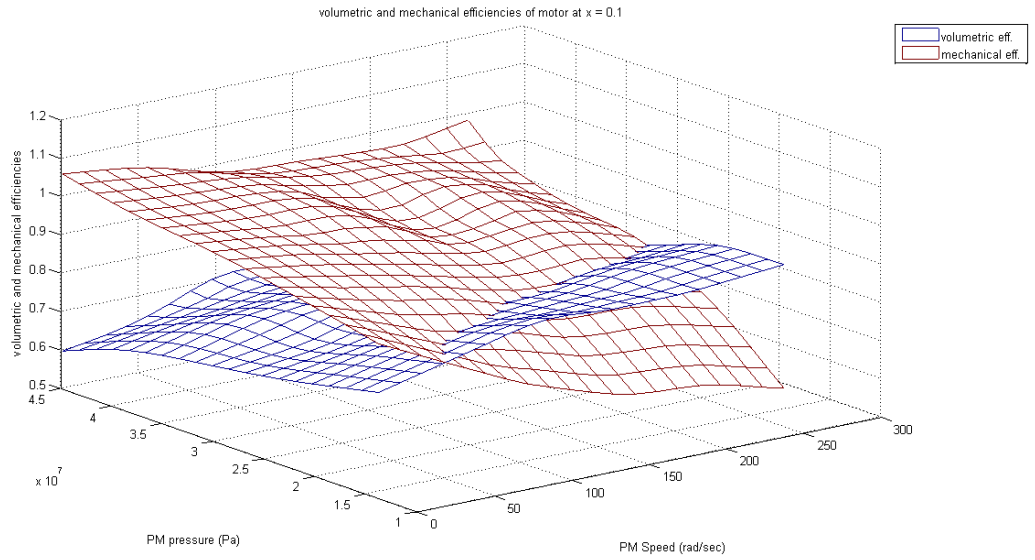
Figure a.5. PM mechanical and volumetric efficiencies in motor mode at x = 1.0

Appendix b. PM efficiency maps in pump mode.
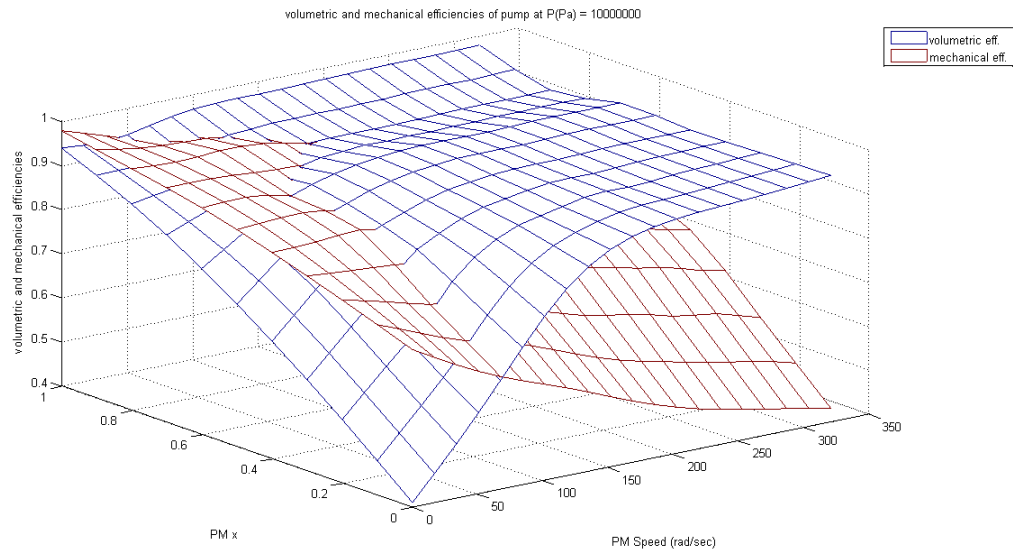
Figure b.1. Pump/ Motor in pump mode efficiency maps at P = 10 Mpa

volumetric and mechanical efficiencies of pump at P(Pa) = 15000000
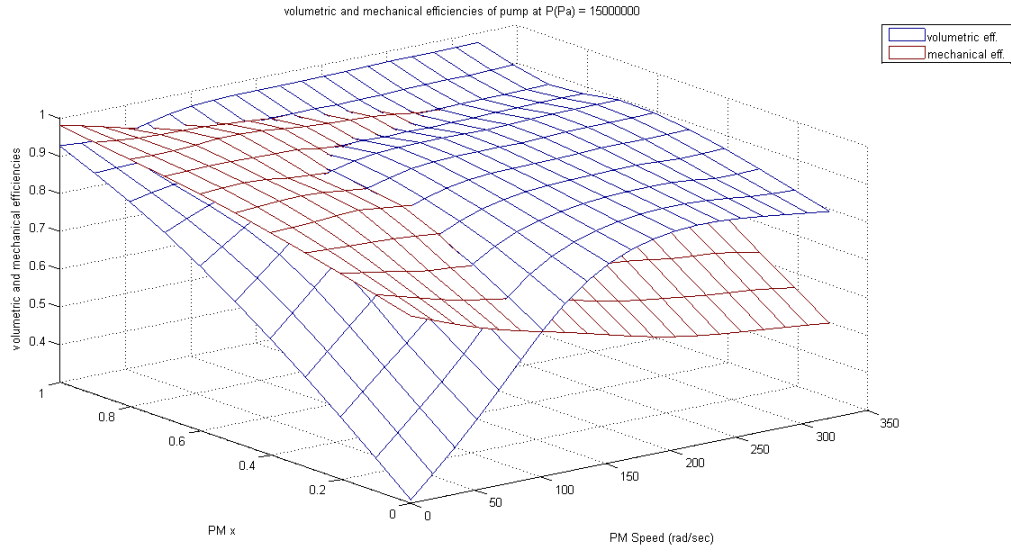
Figure b.2. Pump/ Motor in pump mode efficiency maps at P = 15 Mpa

volumetric and mechanical efficiencies of pump at P(Pa) = 20000000
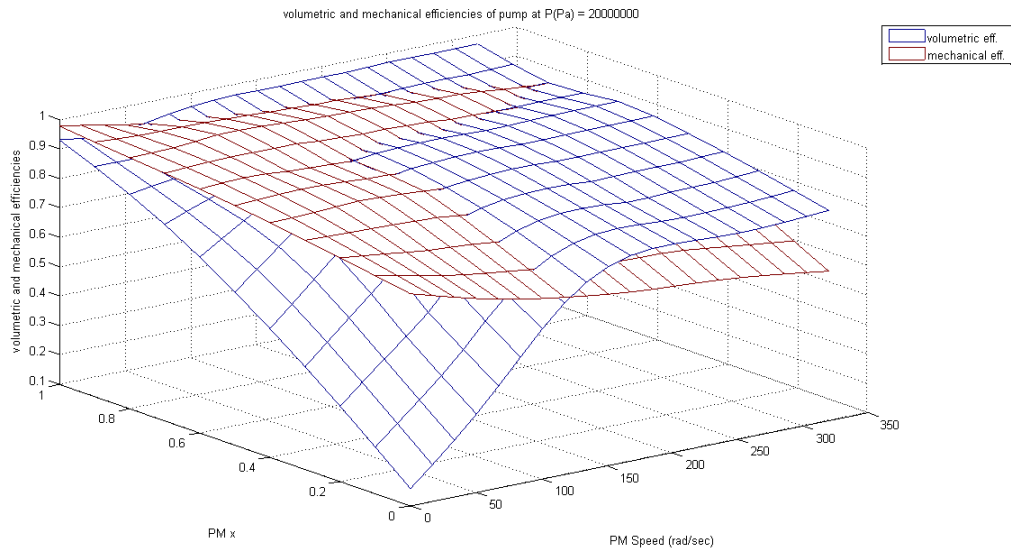
Figure b.3. Pump/ Motor in pump mode efficiency maps at P = 20 Mpa
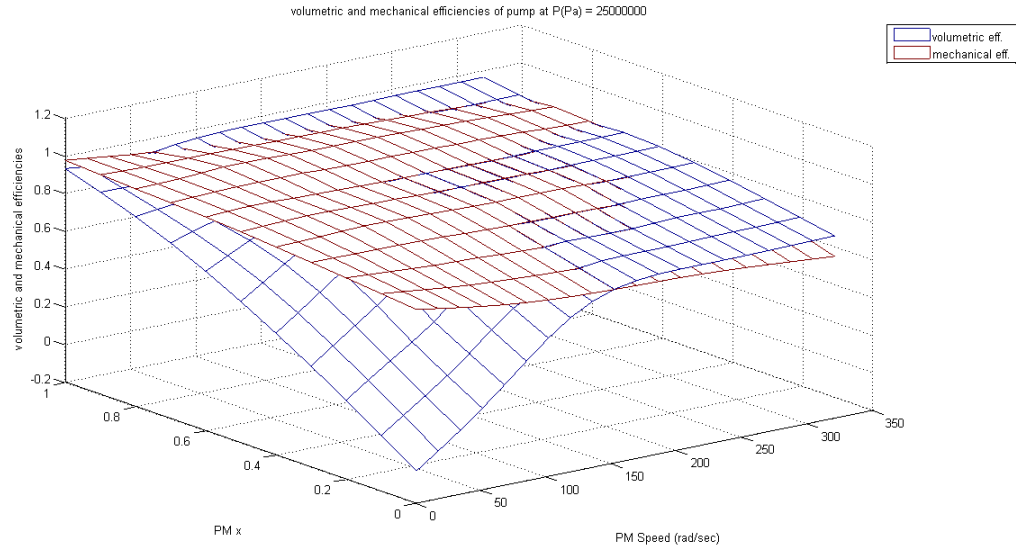
Figure b.4. Pump/ Motor in pump mode efficiency maps at P = 25 Mpa
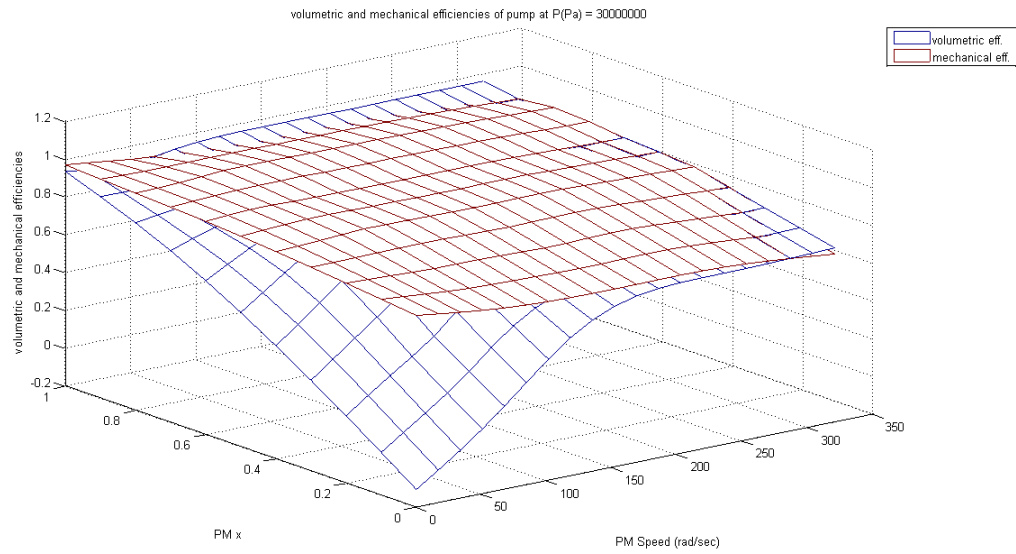
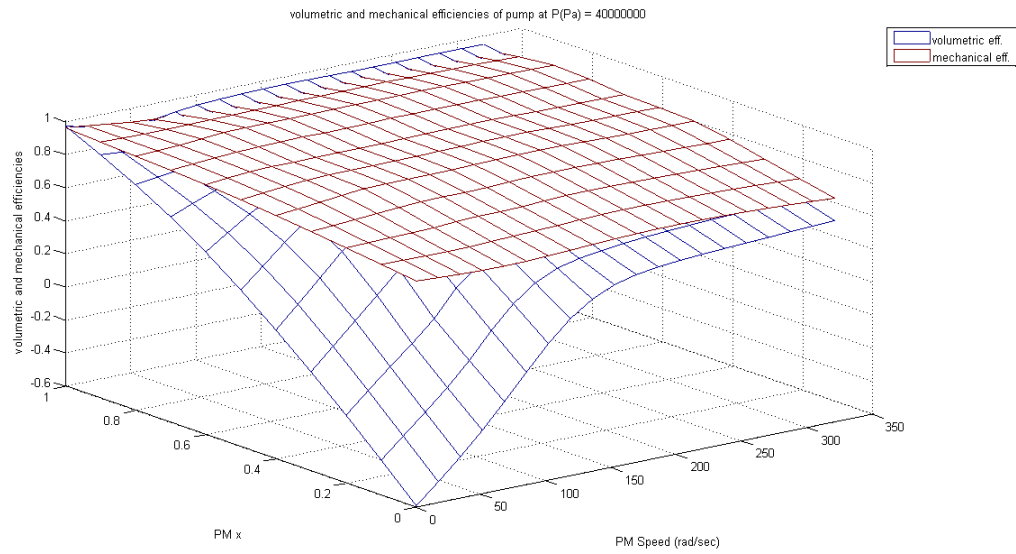**Figure b.5. Pump/ Motor in pump mode efficiency maps at P = 30 Mpa**
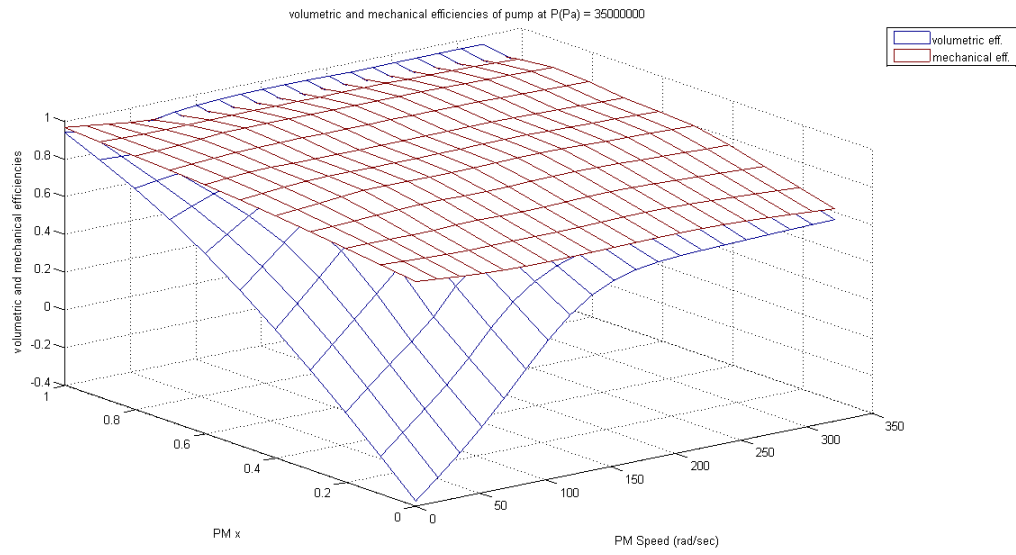
Figure b.6. Pump/ Motor in pump mode efficiency maps at P = 35 Mpa

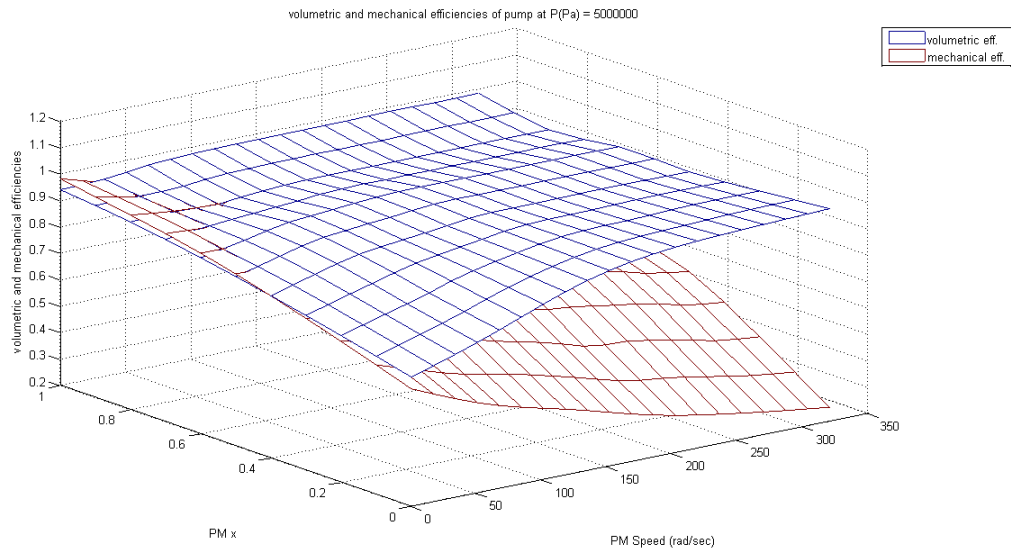**Figure b.7. Pump/ Motor in pump mode efficiency maps at P = 40 Mpa**

Figure b.8. Pump/ Motor in pump mode efficiency maps at P = 50 Mpa

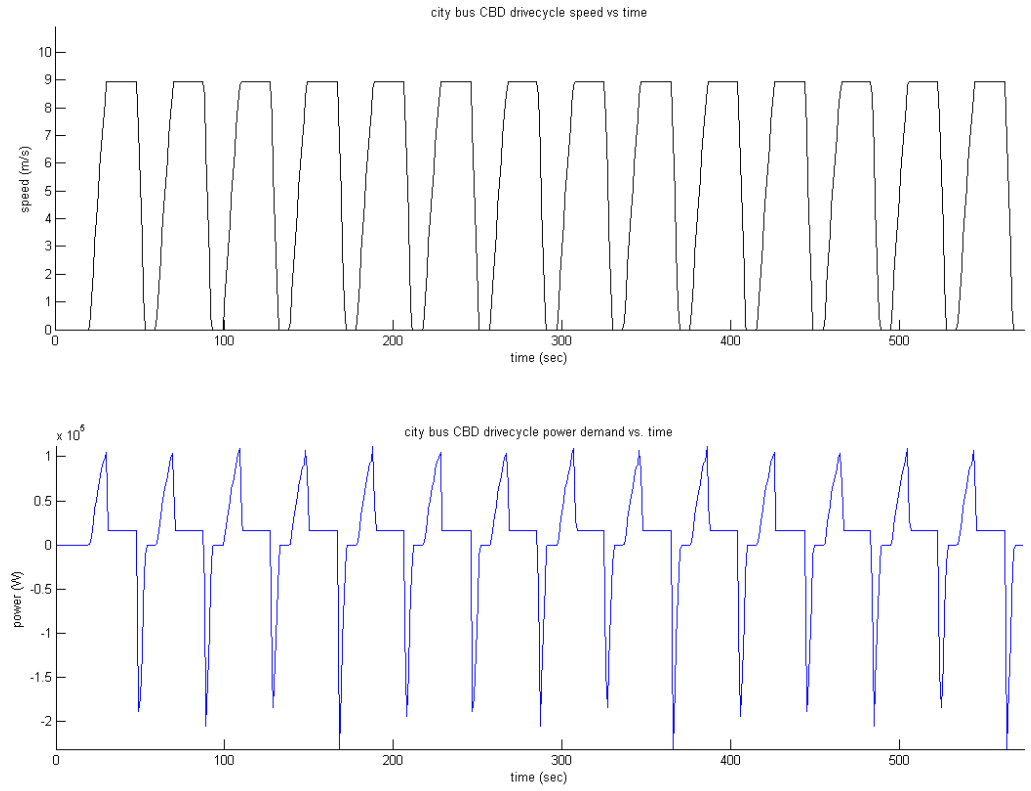## Appendix c. Three city drive cycles and their power demands

city bus CBD drivecycle speed vs time

city bus CBD drivecycle power demand vs. time

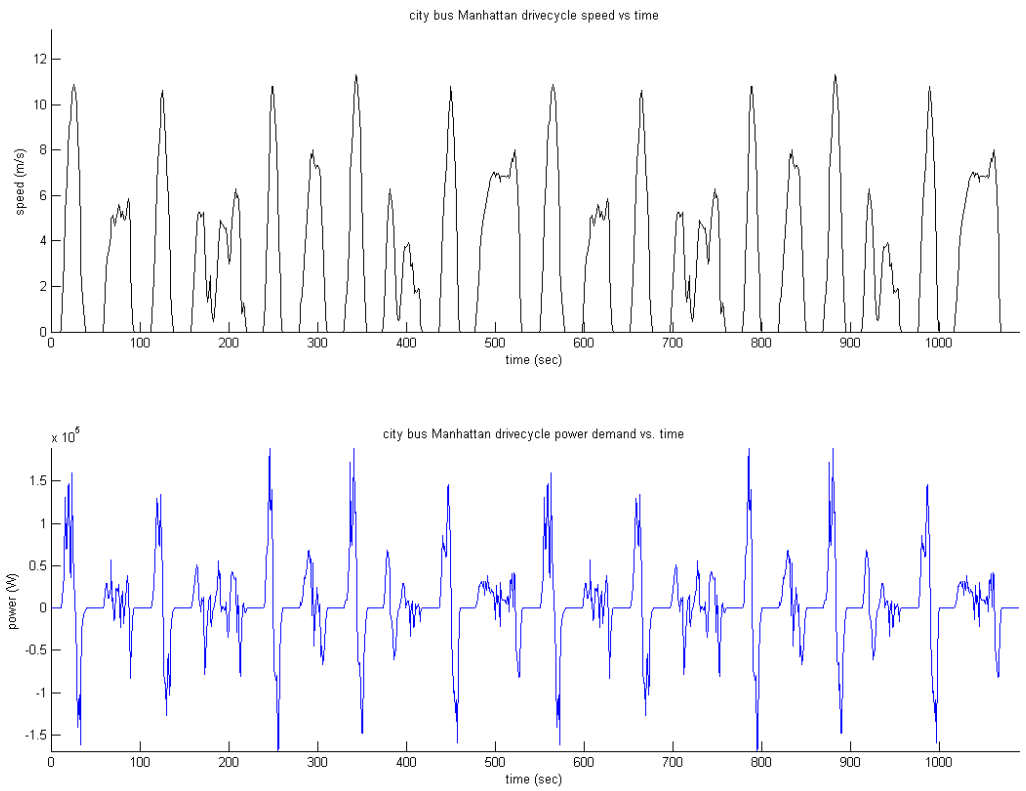**Figure c.1 CBD drive cycle and its power demand**
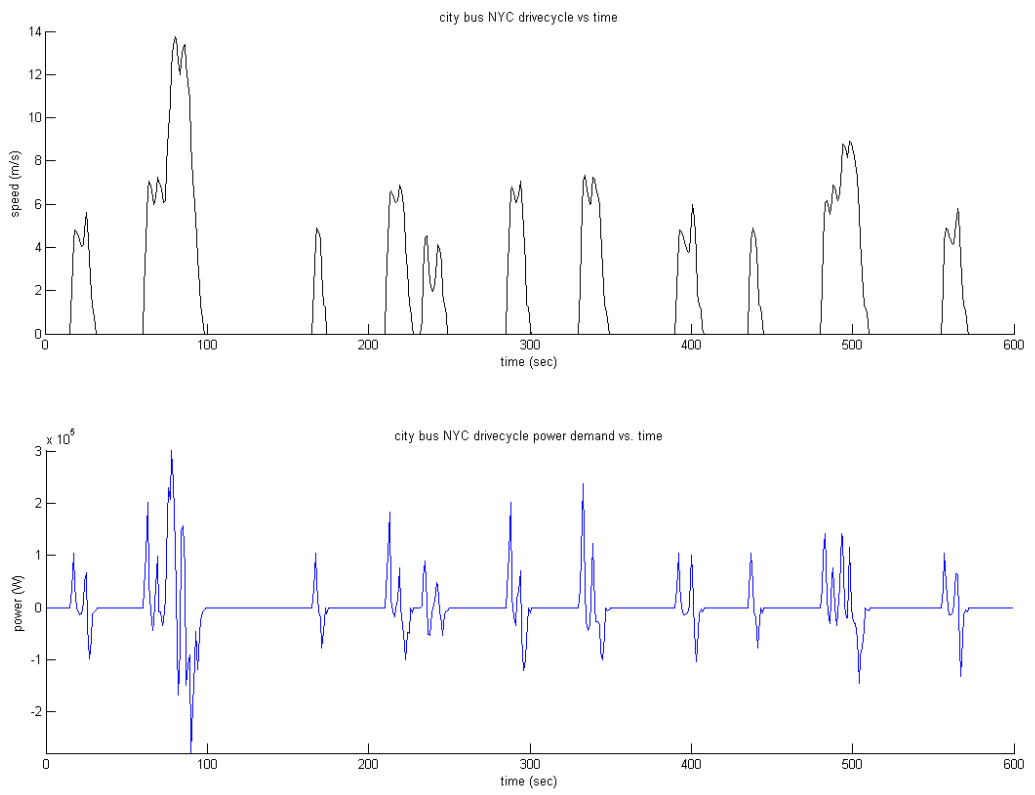
Figure c.2. Manhattan drive cycle and its power demand

Figure c.3. NYC drive cycle and its power demand